Mammalian cell growth characterisation by a non-invasive plate reader assay

nature communications

Article

https://doi.org/10.1038/s41467-023-44396-4

Mammalian cell growth characterisation by a non-invasive plate reader assay

Received: 5 April 2023

Accepted: 12 December 2023

Published online: 02 January 2024

Check for updates

Alice Grob[1,2,7], Chiara Enrico Bena[3,6,7], Roberto Di Blasi[1,2], Daniele Pessina[1], Matthew Sood[1], Zhou Yunyue[4], Carla Bosia[3,5] ✉, Mark Isalan[2,4] ✉ & Francesca Ceroni[1,2] ✉

Automated and non-invasive mammalian cell analysis is currently lagging behind due to a lack of methods suitable for a variety of cell lines and applications. Here, we report the development of a high throughput non-invasive method for tracking mammalian cell growth and performance based on plate reader measurements. We show the method to be suitable for both suspension and adhesion cell lines, and we demonstrate it can be adopted when cells are grown under different environmental conditions. We establish that the method is suitable to inform on effective drug treatments to be used depending on the cell line considered, and that it can support characterisation of engineered mammalian cells over time. This work provides the scientific community with an innovative approach to mammalian cell screening, also contributing to the current efforts towards high throughput and automated mammalian cell engineering.

Recent advances in technology and in the automation of cell screening and engineering have made the design and assembly of large libraries of genetic DNA systems possible in mammalian cells[1–3]. This progress builds upon experimental pipelines that have been established to enable the automation of design-build-test analysis of genetic designs in microbes[4,5]. However, the fast identification of desired variants for various applications is only possible if the behaviour of each construct is assessed in the cellular host. It is important to characterise stability, productivity and performance over time, and a key requirement is to measure the impact on cell growth of different constructs.

Whereas high-throughput growth-tracking methods have been developed for bacterial cells[6], such as simple measurements based on light absorbance[7,8], automated and non-invasive characterisation of both engineered and non-engineered mammalian cells is lagging behind.

Traditional methods for mammalian cell growth characterisation include trypan blue staining, flow-cytometry[9], automated cell counters[10,11] and colorimetric assays[12]. However, these methods are disruptive as they rely on a sample being measured and as such only give a fixed sample measurement in time. Also, they are low throughput and time-consuming, representing a limiting step in the development of high throughput approaches. Protocols that have been developed for indirect counting of mammalian cells include digital holography[13], microscopy[14–17], confluency analysis based on commercially available plate readers[17], adoption of magneto sensors[18] and identification of cell-specific optical density (OD)[19,20]. These are mostly restricted to adherent, monolayered or coated cells, can be expensive and can be limited by the number of samples that one can screen at any one time. The implementation of continuous measurements for both adherent and suspension cells would thus allow for a universal, dynamic, and automated mammalian cell characterisation approach.

To advance the experimental characterisation of mammalian cells, we developed a method for non-invasive, high throughput and automated tracking of mammalian cell growth based on the change in absorbance of the pH indicator phenol red (Fig. 1a). This colour indicator is present in a variety of commonly adopted mammalian growth

[1]Department of Chemical Engineering, Imperial College London, London, UK. [2]Imperial College Centre for Synthetic Biology, Imperial College London, London, UK. [3]Italian Institute for Genomic Medicine, Torino, Italy. [4]Department of Life Sciences, Imperial College London, London, United Kingdom. [5]Department of Applied Science and Technology, Politecnico di Torino, Torino, Italy. [6]Present address: Université Paris-Saclay (INRAE), AgroParisTech, Micalis Institute, 78350 Jouy-en-Josas, France. [7]These authors contributed equally: Alice Grob, Chiara Enrico Bena. ✉e-mail: carla.bosia@polito.it; m.isalan@imperial.ac.uk; f.ceroni@imperial.ac.uk

https://doi.org/10.1038/s41467-023-44396-4

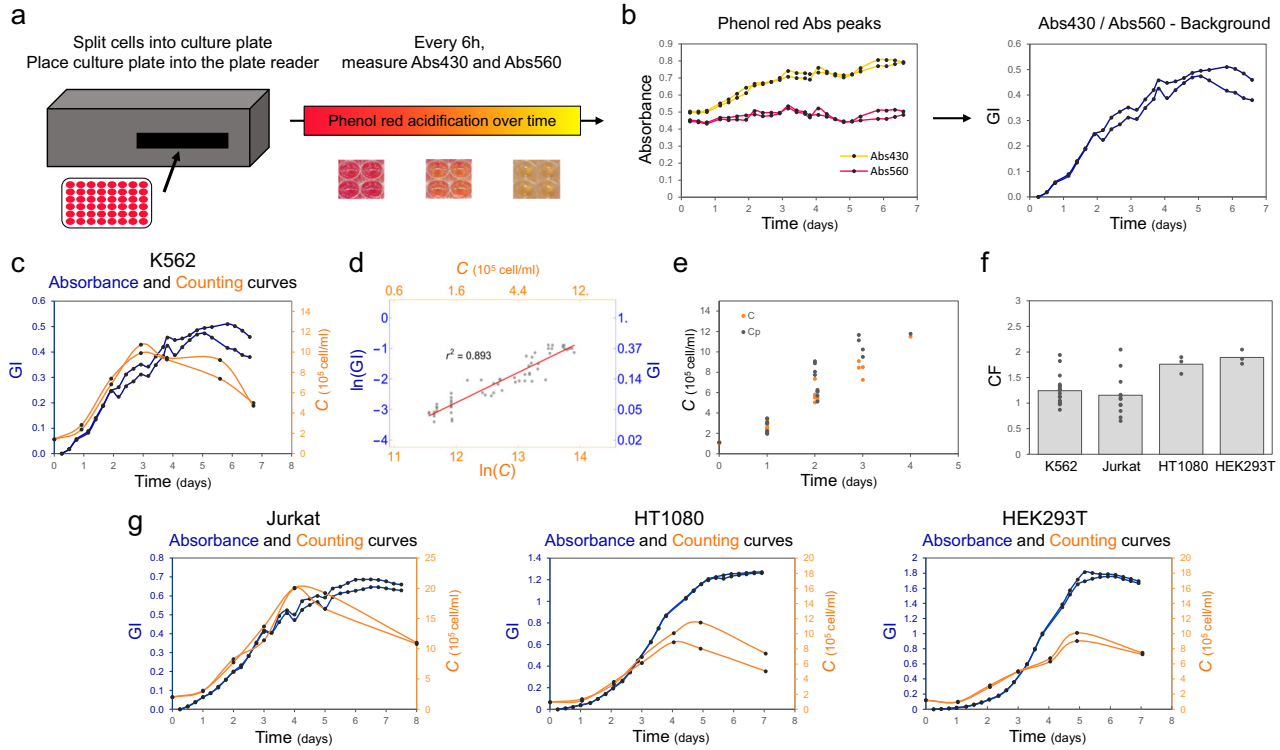

Fig. 1 | A plate-reader assay based on the absorbance of the pH indicator phenol red can be used to dynamically characterise the growth of mammalian cell lines. a Schematic of phenol red-based mammalian growth assay. **b** Representative output of the assay with dynamic of Abs_{430} (yellow) and Abs_{560} (pink) (left). The resulting ratio of Abs_{430} over Abs_{560} normalised to the background yields the growth index (GI) profile over time for K562 cells (right). **c** Representative growth curves resulting from phenol red acidification (GI, blue, left vertical axis) and cell counts (*C*, orange, right vertical axis) of K562 cells. All replicates can be found in Supplementary data file 1. **d** Linear relation between K562 cells ln(GI) and ln(*C*). The red line is the best fit of data within the linear region, i.e. ln(GI) = 0.99*ln(*C*) − 14.6 with a coefficient of determination $r^2 = 0.893$. **e** The data set of GI measurements obtained from K562 cells was split. One subset was used to establish the linear relation between ln(GI) and ln(*C*) while in the other subset *C* was predicted from GI measurement according to the fit shown in panel (**d**), i.e. *C* = (GI/exp(*q*))^(*m*). The resulting predicted *C* (C_p, grey) is plotted here with the measured *C* (*C*, orange) as a function of time. **f** Bar plot of conversion factors (CF) for suspension cells (K562 and Jurkat) and adherent cells (HT1080 and HEK293T). The height of the bar represents the mean value of the single replicates shown as black dots. **g** Representative profiles of GI (blue, left vertical axis) and *C* (orange, right vertical axis) for Jurkat, HT1080 and HEK293T cells. All repeats can be found in Supplementary Data File 1. All CF values can be found in Supplementary Data File 2. The numbers of biological repeats for each sample are reported in Table S3. Data analysis is described in the Methods section and in Supplementary Note 1. Source data are provided as a Source Data file.

media and is available separately as a dye that can be added to any medium of interest[21]. The acidic and basic forms of phenol red are characterised by absorbance peaks at 560 nm and 430 nm (Abs_{560} and Abs_{430}) respectively[22,23]. During mammalian cell growth, phenol red gradually transitions from its basic to its acid form, providing the operator with a quick and visual indication that cells are growing and reaching confluence. Previous work showed that the change in absorbance of phenol red can be used as a valuable method for tracking cell growth in bacteria[24,25] but no one has so far provided a method for mammalian cell tracking using the same principle. Our workflow enables characterisation of mammalian cell growth over time, and we demonstrate this working for both suspension and adhesion cell lines, a clear step forward compared to current state of the art. We also confirm that this method can be adopted for a wide range of applications from routine mammalian cell analysis to a screening of cell sensitivity to drug treatment, but also for the advancement of high throughput characterisation of engineered constructs in these cells, thus making it relevant for both basic and applied research.

Results

A phenol red-based growth assay enables plate reader tracking of mammalian cell growth

We started by considering the suspension cell line K562[26] and designed a routine protocol where cells are first seeded at their recommended seeding density in a 48-well plate. The plate is then inserted into a plate reader where the temperature is set at 37°C and CO_2 at 5%. Absorbance readings for the basic (Abs_{560}) and acidic (Abs_{430}) forms of phenol red are performed every six hours for up to nine days (Fig. 1a).

It was previously suggested for microbes, that a growth index (GI) can be identified by the ratio between Abs_{430} and Abs_{560}[24,25], which yields a characteristic sigmoidal growth profile (Fig. 1b, Fig. S1a–c). To confirm that a GI is also a reliable proxy of cellular growth in mammalian cells, we performed parallel cell counts every 24 hours for each sample, using a standard automated cell counter (see Methods section). We reasoned that this would allow us to compare the growth profiles yielded by the two methods and to benchmark against one of the techniques most adopted for following mammalian cell growth. As expected for batch cell cultures, cell concentration (*C*) yielded a typical sigmoidal curve, inclusive of lag, exponential and stationary phases of growth (Fig. 1c). Plate reader growth curves showed an analogous growth profile (Fig. 1c, Supplementary data file 1).

Specifically, we identified a range for which the logarithm of *C* (ln(*C*)) and the logarithm of GI (ln(GI)) follow a linear relation and that this corresponds to the exponential phase of growth (Fig. 1d, red line, Table S1 and Supplementary Note 1). The slope of the linear fit between ln(GI) and ln(*C*) provides a calibration curve to establish the relation between the actual number of cells and the detected absorbance ratio (ln(GI) = *m**ln(*C*) + *q*, Table S2). For K562 cells, a slope value close to 1 (i.e. 0.99) suggests that *GI* scales almost

linearly with C (see Table S2 and Supplementary Note 1). Moreover, from the relation existing between ln(GI) and ln(C), C can be estimated from GI as (GI/exp(q))^(1/m) (Supplementary Note 1). Thus, to fully benchmark our method against cell counts, we decided to use a data subset to establish the relation between C and GI and use it to predict C (C_p) from GI in the remaining data subset in exponential phase (Fig. 1e). C_p values overlap with actual C values over time, confirming the relation existing between ln(GI) and ln(C) in exponential phase.

Thanks to this relation, it was also possible to compute the growth rate from plate reader (μ_p) and cell counts (μ_c) in the same way, i.e. by computing the slope of the data within the exponential phase as a function of time (Supplementary data file 2 and Supplementary Note 1 for data analysis details). In order to establish the relationship between μ_p and μ_c, we developed a protocol for automated analysis that enabled the calculation of the growth rate from each dataset (see Supplementary Note 1 and Supplementary software file). We named the conversion factor (CF) the ratio between μ_p and μ_c. We found that CF for K562 cells is around 1, suggesting that the indirect μ_p computed through GI is a proxy for the effective μ_c of the population obtained by direct cell counting (Fig. 1f, Supplementary data file 2 and Supplementary Note 2). This relation is valid within the exponential phase, when μ_c and μ_p scale linearly to each other, as shown in Fig. 1d. Analogously to the relation observed in bacteria between OD and cell concentration[8], linearity between the two quantities is lost when cells start saturating. As evident from Fig. 1c, after saturation, the growth curve for C decreases more rapidly than the one for GI.

Taken together these results demonstrate that a phenol red-based plate reader assay allows tracking of mammalian cells growth in standard conditions and that C_p and μ_p computed through GI are accurate proxies for C and μ_c respectively.

Suspension and adhesion cell lines can be characterised by plate reader-based analysis

We next set out to verify whether it was possible to apply this method to a range of cell lines, and specifically to both suspension and adherent cells. We thus adapted our protocol to characterise the growth of a second suspension cell line (Jurkat[27]) and two cell lines growing in adhesion (HT1080[28] and HEK293T[29]). As shown in Fig. 1f, when the cells are grown in standard growth medium at 37 °C, GI captures the trend of the growth profiles of all cell types reliably (Fig. 1g, Fig. S1d–f, Fig. S2), again leading to a linear relation between ln(GI) and ln(C), within the exponential phase of growth (Fig. S3, Tables S1 and S2). When we compared the CF for the four different cell lines, we noticed that the CF for Jurkat cells is also close to 1, as for K562 cells, while both adhesion cell lines show an average CF closer to 2 (Fig. 1f, Table S4 and Supplementary Note 1). To explain this difference, we considered that both K562 and Jurkat cells are cultured in RPMI medium (containing 5 mg/L phenol red), while HT1080 and HEK293T cells are cultured in DMEM (containing 15 mg/L phenol red). Indeed, we noticed that Abs_{560} follows a very different trend for cells grown in DMEM (Fig. S2a, b), compared to RPMI (Fig. S1a, b), with a more pronounced decreased over time in the former case. This is then reflected in a wider GI variation (Fig. S2e, f). It was previously suggested that DMEM, and specifically Abs_{560} in this medium, is more sensitive to pH change if compared to RPMI, leading to the hypothesis that the difference in CF is directly linked to a medium-dependent effect that leads to a different profile in Abs_{560}[30].

To test this experimentally, we purchased DMEM where no phenol red is present and considered HT1080 cells growing in DMEM supplemented with 15 mg/L phenol red for reference, as in the original DMEM formulation adopted in the experiments presented in this manuscript and in DMEM supplemented with 5 mg/L of phenol red, same concentration present in other commercially available media, like the RPMI adopted to grow the suspension cell lines of this study. Cell growth was not affected by phenol red concentration as displayed by the cell counts (Fig. S4a). When considering GI, we confirmed that in the presence of 15 mg/L phenol red, GI saturates at a higher value and with a higher average growth rate when compared to the case of 5 mg/L (Fig. S4b–e). Linearity is not impacted (r^2 = 0.91 for 15 mg/l and 0.95 for 5 mg/l) and a corresponding CF can be identified, similar to what previously shown in Fig. 1e (Fig. S4f, g). CF for HT1080 growing with 15 mg/L phenol red is consistent with the one previously obtained in Fig. 1e. For HT1080 growing with 5 mg/L phenol red, the average CF drops to a range compatible with what previously observed for suspension cell lines grown in RPMI. This additional data set suggests that CF may indeed depend on the experimental condition, and possibly the cell line, adopted in the assay. Nonetheless, it also confirms that a linear relation can be found between ln(GI) and ln(C) when the cell line is initially characterised.

Overall, we confirmed that, like other methods routinely adopted in cell and molecular biology (e.g. bacterial OD[8], protein quantification), the workflow requires an initial calibration curve for identification of the linear relation between ln(GI) and ln(C). Once this is obtained, μ_p can be treated and considered as a direct proxy for the actual cellular μ_c, making the method generalisable for both suspension and adhesion cells.

Phenol red-based growth assay enables mammalian growth tracking under different conditions

Once we established that our method could reliably follow the growth profiles of different cell types, we investigated if it could be adopted for the characterisation of cell growth across different culture conditions. Temperature and carbon source are two key parameters in mammalian process optimisation, and they have been previously shown to impact bioproduction and therapeutic applications[31–33]. Proving that our protocol is robust to varying environmental conditions is thus an essential requirement to confirm it can be applied to wider mammalian cell analysis.

We focused on comparing K562 and Jurkat cells growing at 37°C and 33°C, in the presence of glucose (Glu) or mannose (Man) (Fig. 2 and Fig. S5). GI profiles still reliably captured cell count profiles, for both cell lines growing at 33°C (Fig. 2a and S5a) and when Man was used as carbon source (Fig. 2b, c, S5b and c). Data analysis by our automated pipeline confirmed that changing growth conditions did not affect the linear relation previously observed between ln(GI) and ln(C) (Fig. 2d–f and S5d–f). Importantly, the average value of CF for both cell lines did not change (Fig. S6a, Table S5 and Supplementary data file 2). Based on these results, we decided to verify once again how automatable our pipeline is and verify if, once we established GI, μ_p and CF for a given cell line and condition, it could be possible to infer μ_c for subsequent experiments where only plate reader measures of GI are performed in the same conditions. We thus used the calculated μ_p and CF from an initial set of measures for K562 and Jurkat cells growing at 37°C and 33°C, in the presence of Glu or Man, to estimate μ_c for subsequent plate reader runs and compared the estimated values (μ_{cp}) with the actual μ_c calculated by parallel cell counting (Fig. S6b). μ_{cp} closely matched the measured μ_c, thus confirming that once an initial characterisation is performed, the identified CF can be adopted to infer information on actual μ_c of the cells in further experiments without the need for cell counting.

High throughput screening of therapeutic drugs enables identification of cell line-specific response

Doxorubicin (doxo) is a well-known chemotherapeutic agent adopted in anticancer medications to treat, amongst others, breast cancer and leukaemia[34]. Doxo inhibits cell growth via interference with DNA replication and RNA synthesis, leading to cell death[35]. Here, we set to use doxo as testbed to investigate the suitability of our workflow for testing the effect of drug treatment on mammalian cells. Indeed, while

https://doi.org/10.1038/s41467-023-44396-4

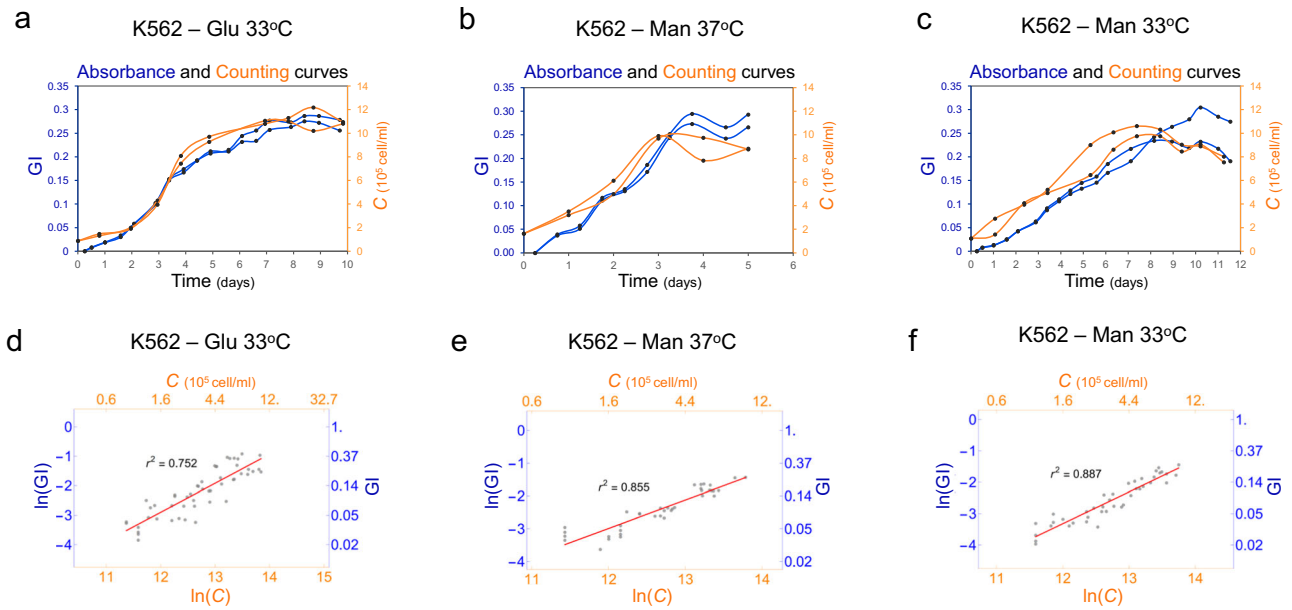

Fig. 2 | Growth of mammalian cell lines under different conditions can be characterised by a plate reader assay. Representative growth index (GI, blue, left vertical axis) and cell count (*C*, orange, right vertical axis) profiles over time of K562 cells grown with glucose (Glu) **a** at 33°C or mannose (Man) at either **b** 37°C or **c** 33°C. All replicates can be found in Supplementary data file 1. Linear relation for ln(GI) and ln(*C*) of K562 cells grown with Glu **d** at 33°C or Man at either **e** 37°C or **f** 33°C, indicating r^2 values of 0.752, 0.855 and 0.887 in exponential phase, respectively. Red solid lines correspond to the linear fit. Fit equations are reported in Table S2. The numbers of biological repeats for each sample are reported in Table S3. Data analysis is described in the Methods section and in Supplementary Note 1. Source data are provided as a Source Data file.

traditional methods for identification of effective doxo concentrations, and for screening sensitivity of different cell lines to the drug, involve manual or automated cell counting, we reasoned that our platform could provide an improved workflow for high throughput testing.

To investigate this, we first verified that the addition of chemicals to the culture medium does not affect GI over time. For this purpose, we supplemented RPMI and DMEM with doxo, as well as with other commonly adopted inducer molecules (doxycycline, dox; and IPTG), antibiotics (blasticidin, blast; puromycin, puro; and hygromycin B, HygB) and the drug solvent DMSO. The addition of these compounds had no impact on medium acidification over time as shown in Fig. S7.

We then moved forward to apply our protocol to test the effect of different doxo concentrations on two of the four cell lines considered, namely HT1080 (known to be doxo sensitive[36,37]), and K562, selected as testbed of a leukaemia cell line[26]. Both cell lines were treated with 0, 10, 25, 50, 75, 100, 500, 750 nM and 1uM Doxo, added at 24 hours after the start of the assay, and parallel GI measurements and cell counting were performed (Fig. 3a, b). We confirmed that μ_p and μ_c displayed a similar decreasing trend for increasing doxo concentrations in both cell lines as shown by the regression lines in Fig. 3c, d with angular coefficients of −15.887 and −16.414 for μ_p and μ_c in HT1080, respectively, and −20.212 and −19.296 for μ_p and μ_c in K562, respectively. Furthermore, it as possible to identify a specific cell line response to doxo treatment. Indeed, HT1080 cells treated with 75 nM doxo resulted in an average 30% decrease of μ_p and 84% decrease of μ_c, whereas K562 cells displayed less sensitivity to the same doxo treatment with an average 17% decrease of μ_p and 33% decrease of μ_c compared to the untreated control.

Finally, while analysing the data, we noticed that, for increasing concentrations of doxo, both GI and cell count curves flatten, as a reflection of cell death (Fig. 3 and Supplementary data file 1). This led to a more difficult estimation of μ_p and μ_c, due to a less pronounced exponential phase of growth needed to estimate both the linearity region and growth rates (see Supplementary Note 1). As previously shown for bacteria, treatment with molecules that affect cell viability may impact such linearity[8]. This needs to be considered as it may lead to the case where the assay is qualitatively very useful but is only semi-quantitative.

To corroborate these results, we considered Jurkat cells treated with the microtubule inhibitor colchicine, an inhibitor of cell division that, similarly to doxo, impacts cell growth[38]. GI measurement and parallel counting were performed for cells treated and untreated with 0.025ug/ml colchicine 24 hours after the start of the assay (Fig. S8). Results showed that after colchicine addition, μ_c decreased by ~100% in treated cells compared to cell growth rate before treatment, while μ_p decreased by ~75% (Fig. S8). This reflective change of μ_p indicated that GI curves can again capture changes in growth rate occurring over the duration of the assay thus mirroring the cell counts. To conclude, while our proposed assay is mainly suitable for actively growing cells for which a linearity window can easily be identified, it still can be adopted for semi-quantitative characterisation of the dose-response effect of drug treatments on mammalian cell viability with a throughput difficult to achieve with standard cell counting approaches.

Automated tracking of engineered mammalian cells and single cell construct performance

Finally, we thought to apply our method to the characterisation of engineered mammalian cells, considering that high throughput and automated analysis of engineered hosts is much needed within the biotechnology and synthetic biology communities. To provide proof-of-concept of the suitability of our method for this task, the HEK293TLP-EBFP cell line, a HEK293T cell line bearing a landing pad (LP) cassette integrated in the AAVS1 locus (available from Matreyek et al.[39]) was selected. The LP cassette codes for an EBFP expressed under an inducible Tet promoter. The LP also bears a second transcriptional unit expressing the rtTA transactivator under the control of a constitutive EF1α promoter (Fig. 4a). When doxycycline (dox) is present, the rtTA transcription factor activates the Tet promoter and EBFP is expressed. Conversely, when dox is absent, the cassette is off. Since

https://doi.org/10.1038/s41467-023-44396-4

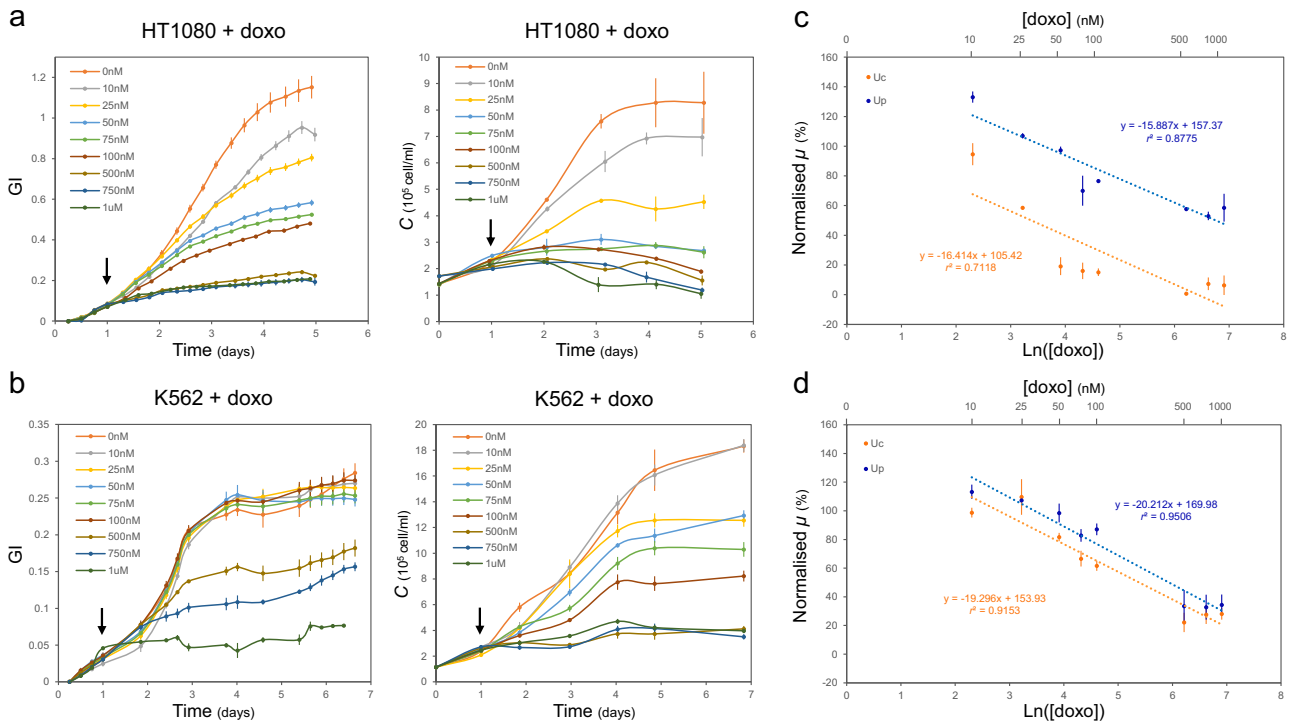

Fig. 3 | Growth of mammalian cell lines treated with doxorubicin can be characterised by a plate reader assay. Response of HT1080 (**a**) and K562 (**b**) cells to treatment with increasing doxorubicin (doxo) concentrations (0 nM to 1 μM). Doxo was added 24 hours after the start of the assay (arrow). Relative growth rates form plate reader assay (μ_p, blue) and cell counts (μ_c, orange) of HT1080 (**c**) and K562 (**d**) cells treated with 0nM-1μM doxo (axis in log scale) were normalized to the average value of μ_p and μ_c for cells treated with 0 nM doxo. Dashed blue and orange lines indicate the variation trend of μ_p and μ_c respectively for cells treated with 10 nM to 1 μM doxo. Equation and r^2 values of these trendline are indicated. Number of biological repeats for each sample are reported in Table S3. Data are presented as mean values +/- SEM. Data analysis is described in the methods section and in Supplementary Note 1. All repeats can be found in Supplementary data file 1. Source data are provided as a Source Data file.

the switch is known to be sensitive to different dox levels, we reasoned it could work as a good proxy for genomic constructs with different expression strengths, thus providing a good testbed for our method.

Firstly, we characterised the HEK293TLP-EBFP cell line by following our protocol as outlined in Fig. 1a (Fig. S9a–c). Performing plate reader measurements and cell counts in parallel (Fig. S9d), we confirmed linearity between ln(GI) and ln(C) for this additional cell line (Fig. S9e) and established its specific CF (Fig. S9f).

We then reasoned that the presence of phenol red in the medium could impact fluorescence readout. Thus, before assessing the fluorescence response of the cell line, we assessed if crosstalk could be detected between phenol red and fluorescence readings. In order to do so, we expanded the analysis to a second cell line, HEK293TLP-mCherry, developed in-house. Similarly to HEK293LP-EBFP, HEK293TLP-mCherry codes for a mCherry protein under the control of dox induction (see EBFP diagram in Fig. S4a and Source data for sequence). By assessing fluorescence per cell in the presence and absence of phenol red, we confirmed that the presence of phenol red in the medium does not impact the fluorescence readout (Fig. S10).

Once the suitability of the workflow was confirmed, we further characterised the response of the HEK293LP-EBFP cell line to dox induction. To do so, cells were seeded in a 48-well plate and were allowed to grow in the plate reader for one week after induction at T0 with different concentrations of dox. GI for the different samples and total EBFP fluorescence were captured (Fig. 4b, c). As expected, increased dox induction led to increasing EBFP levels.

Bacterial OD is routinely used to infer normalised protein expression per cell. This is an essential practice to compare samples and conditions, as it enables us to take differences in growth and in cell number into account when characterisation of a construct functionality is sought. Thus, we thought to calculate the C_p value corresponding to a given GI value (Fig. 4d), similarly to what we previously did in Fig. 1e (see Supplementary Note 1 for details). We then compared how accurate the prediction of C from GI is compared to bacterial OD. We compared the mean C_p by our calibration method to the mean measured C which reduces to the accuracy defined as $A = C_p/C$. The closer A is to 1, the more accurate the method is in estimating cell counts. We identified a similar accuracy in our approach compared to the accuracy of OD measurements. Indeed, for K562 cells, A equals (1.07 + /− 0.02), in agreement with the accuracy defined for bacterial cells[40]. The procedure and results of the accuracy calculations can be found in Supplementary Note 3. Once we had confirmed the accuracy of our approach, we adopted the calculate C_p for the HEK293TLP-EBFP cell assays to normalise the protein expression on the estimated number of cells at a given moment in time (i.e. three days), within the linearity window, and obtain an estimated quantitative measure of expression levels per cell (Fig. 4e). In the work published by Matreyek et al., authors performed flow cytometry measurements and characterisation of the induction dynamic of the HEK293LP-EBFP cell line, looking at EBFP signal expression over time. They monitored that cells induced with 2 ng/μl dox displayed an increase in EBFP expression per cell up to five days. Our normalised EBFP data (Fig. S11) show a similar increase in EBFP per cell over time after induction. In conclusion, our method led us to similar single-cell construct characterisation but via a non-invasive and high throughput method that enabled both growth and fluorescence tracking with no requirement for manual handling.

Discussion

The ability to track mammalian cell growth and performance over time, adopting automated and non-invasive protocols, is key to

https://doi.org/10.1038/s41467-023-44396-4

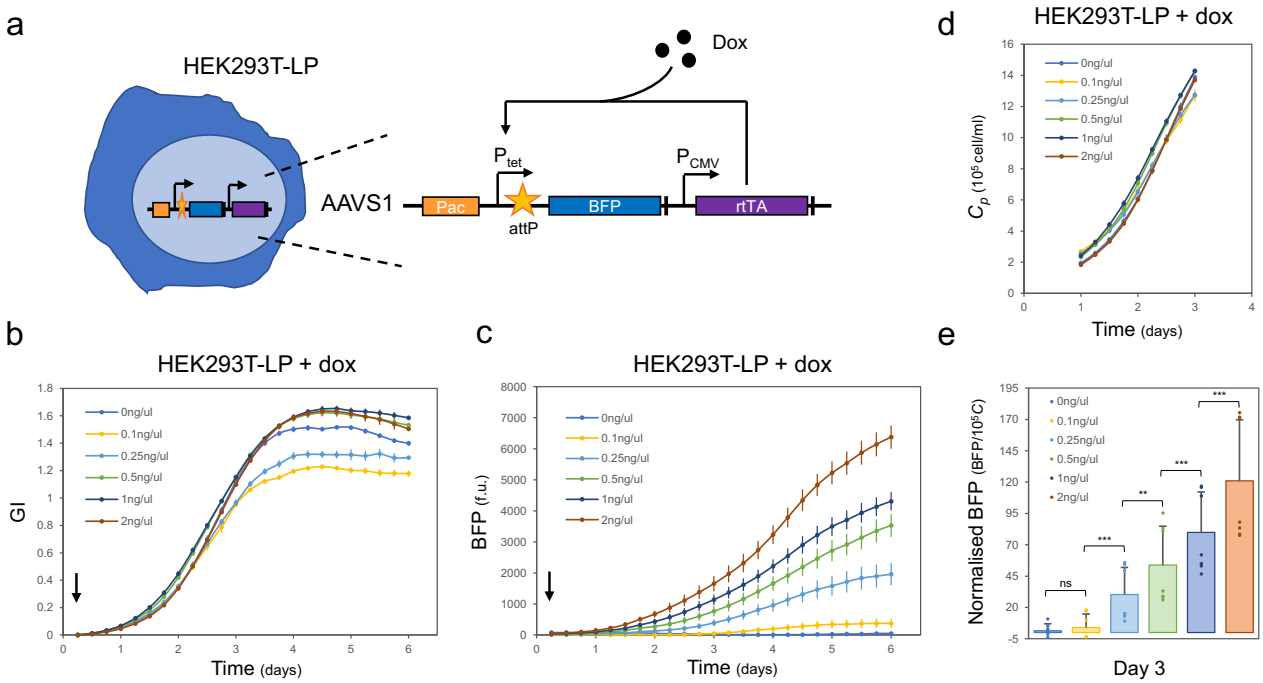

Fig. 4 | Gene expression from a landing pad cassette integrated in HEK293T cells can be characterised over time with a plate reader assay. **a** Schematic of the landing pad (LP) in HEK293TLP-EBFP cell line from Matreyek et al.[39]. A cassette expressing the dox-responsive rtTA transactivator and the inducible Ptet-EBFP transcriptional unit is integrated into the AAVS1 locus of HEK293T cells. **b** growth index (GI) and **c** EBFP fluorescence of HEK293LP-EBFP cells can be followed over a one-week time frame for samples induced with increasing concentrations of dox (0 ng/µl to 2 ng/µl). The addition of dox at T0 is indicated by an arrow. **d** Estimated *C* (C_p), derived from *GI*, within the linear time frame between the two variables (i.e. one to three days). **e** Bar plot of fluorescence per cell, calculated by normalising the total EBFP fluorescence on the estimated *C*, at three days post induction. Data are presented as mean values +/- SD with single replicates shown as dots. A two-sided t-test indicated that normalised EBFP levels increase significantly in cells treated with 0.25 ng/µl dox and above (ns, non-significant: $p > 0.5$, **: $p < 0.01$ and ***: $p < 0.001$). Numbers of biological repeats for each sample are reported in Table S3. Data analysis is described in the Methods section and in Supplementary Note 1. Exact p values and source data are provided as a Source Data file.

support current advances in mammalian cell research. In this study, we developed a first-of-its-kind plate-based high throughput method for the characterisation of mammalian cell growth. The method is based on the change in absorbance observed for the colour indicator phenol red during growth in mammalian cultures. It consists of four main steps, in which (i) cells are first seeded with a desired concentration and growth medium into a 48-well plate that is then inserted into a plate reader with temperature and CO_2 control; (ii) measurements of Abs_{430} and Abs_{560} are performed every six hours for one week; (iii) a ratio of these absorbances is computed in order to generate a GI curve; (iv) automated data analysis is used to identify the growth rate of the GI curve in exponential phase. An initial calibration is required for any new cell line to be analysed, and this can be done by performing cell counts every 24 hours in parallel to the initial plate reader measurements. The workflow then supports analysis of the cell counts and plate reader curves to identify their corresponding growth rates. The resulting ratio between the calculated growth rate in a plate reader, μ_p, and the growth rate from cell counts, μ_c, defines a conversion factor, CF, which holds in exponential phase, i.e. when ln(GI) and ln(*C*) scale linearly. We showed that, for each growth curve, CF is compatible to the slope of the linear relation between ln(GI) and ln(*C*).

We started by showing that our method enables tracking of both suspension and adhesion cell lines, going beyond existing methods currently restricted to one of the two cell types[15,17]. We then showed that together with standard growing conditions, the method can be used to characterise cell growth and performance when temperature and medium composition are changed. The method also successfully provides characterisation of cell-specific responses to chemotherapeutic drug treatment and identification of effective working drug concentrations. However, when chemical agents are adopted that impact cell growth, the linearity between ln(GI) and ln(*C*) may be affected as previously reported for bacterial OD[8]. While this may impact the quantitative power of the approach, we showed that GI still closely follows the trend of cell counts, providing a useful workflow for high throughput analysis of cell viability.

When comparing our approach to OD, it must also be considered that, while OD is based on the measurement of scattered light from cells in solution, GI in our workflow is based on media acidification. Thus, GI is a dynamic measurement of mammalian cell growth dependent on the conditions and history of growth, while OD enables assessment of cell concentration at any given moment in time, independently of the history of the cell population.

Finally, we demonstrated that engineered mammalian cells can be characterised in their growth and fluorescent outputs when an integrated cassette is expressed. This will need to account for an initial screen to ensure no crosstalk is present between a given fluorescent protein and phenol red in the medium, as shown by our data for EBFP and mCherry. Importantly, we provide evidence that, once an initial calibration is established for a given cell line in a specific condition, the method can be adopted to infer actual μ_c and cell numbers from plate reader measurements alone. By adopting the relation existing between GI and *C* to convert plate reader data into cell counts, the protocol enables quantification of construct and cell performance over time when different induction is sought. This strengthens the relevance of the methods widening its potential applications in mammalian cell analysis.

Our method has the potential to greatly support advancements in the automation of mammalian cell screening both in basic and applied research. For the latter, while for several micro-organisms it is now possible to perform automated library assembly and parallel testing of

high number of variants[41–43], the uptake of the same workflow in mammalian cells is lagging behind. Design and assembly of large construct libraries is now possible for mammalian systems thanks to the development of toolkits that support modular and high throughput construct generation[44,45], but the screening of such variants within their target host is slowed down by the low throughput protocols that were previously available. Biofoundries have been created over the last decade to address this need, specifically aiming to introduce automation into the well-known design-build-test cycle of synthetic biology[46]. In parallel, important technological advances have arisen, like the ones showcased by companies such as Berkley Lights that allow automated cell line development and clone selection[47,48]. However, such technologies are still currently inaccessible to lab-end users, due to their high costs and need for dedicated lab space.

Methods which are more easily accessible, such as the one developed here, will thus be pivotal in supporting the advancement of mammalian cell analysis, and in enabling a more dynamic, automated and higher throughput characterisation of mammalian cells than was thus far possible.

Methods

Cell culture

Suspension cells [K562 (ATCC CCL-243) and Jurkat (ATCC TIB-152)] and adherent cells [HT1080 (ATCC CCL-121), HEK293T (ATCC CRL-3216), HEK293TLP-EBFP (HEK 293T AAVS1 LP, kind gift from D.M. Fowler), HEK293TLP-mCherry (bearing genomic expression of mCherry, generated in-house, see Source data for map and sequence) were cultured respectively in RPMI medium 1640 (Gibco A10491-01) or DMEM medium (Gibco 31966-021) with 10% foetal bovine serum (FBS; Gibco). As per ATCC guidelines K562 and Jurkat cell lines do not require continuous shaking. To assess the effect of phenol red concentration, HT1080 cell were cultured in clear DMEM (Gibco 21063-029) supplemented with 15 mg/L or 5 mg/L phenol red (Sigma). For characterisation of growth in different conditions, suspension and adherent cells were pre-cultured for two weeks in their respective glucose-free medium (Gibco 11879-020) with 10% FBS and 25 mM Man (Sigma). This concentration of Man was also adopted for plate base and cell count measurements.

Plate reader assay

Suspension and adherent cells were resuspended in fresh medium at 10^5 cells/ml and plated into a 48-well plate (Greiner). To limit evaporation, phosphate-buffered saline (PBS; Sigma-Aldrich) was added in-between wells and the plate was sealed with parafilm on its long sides, leaving the short sides for CO_2 exchange. The plate was then placed in a SPARK or an Infinite M200 Pro microplate reader (Tecan) and incubated at 33 °C or 37 °C ± 0.5 with 5% ± 0.5 CO2 for up to 15 days. Every six hours, the plate of suspension cells was orbitally shaken for 20 seconds at 2.5 mm amplitude, incubated for 5 seconds and then Abs_{430} and Abs_{560} were measured. For adherent cells, Abs_{430} and Abs_{560} were measured every six hours without shaking.

Cell counting

Cell counting was performed in parallel to the plate reader assay. Every 24 hours, the 48 well plate was taken out of the microplate reader, 5 µl of suspension cells were stained with 0.2% trypan blue (Gibco) and counted using a TC20™ automated cell counter (Bio-Rad). Adherent cells were detached using 0.05% Trypsin-EDTA (Gibco) then inactivated by v/v DMEM medium. Cell counting of these cells was performed using a Nucleocounter NC-250™ (Chemometec). The remaining cells were removed from the well and replaced by PBS to minimise evaporation. Subsequently, the plate was sealed again with parafilm on its long sides and replaced inside the microplate reader prior to restarting the plate reader assay.

Growth curves

For suspension cell lines, cell counting, and absorbance measurements were performed from the same well, from seeding to saturation. Thus, the growth curves obtained for these cells correspond to measurements over time from a single well. On the contrary, for adherent cells, each time point corresponds to a different well due to the need for trypsinization and detachment of the cells before counting. For both C and GI growth curves each time point thus corresponds to the measurement of a given well at a given time. In parallel to the wells used for counting adhesion cells, two wells were solely measured by plate reader for the entire duration of the experiment. GI values were normalised to their initial values at six hours, GI_0 (see Supplementary Note 1) and subsequent first measurements upon restarting the plate reader were discarded.

Bacterial OD600 accuracy assay

The following protocol was followed to perform the first of the two analysis methods presented in detail in Supplementary Note 3. *E. coli* DH10B cells were grown at 37 °C overnight with aeration in a shaking incubator in 5 ml of M9 medium [M9 salts supplemented with 0.4% casamino acids (MP Biomedical), 0.25 mg/ml thiamine hydrochloride (Sigma), 2 mM MgSO4 (Sigma), 0.1 mM CaCl2 (WR), 0.4% fructose (Sigma)] ($n = 6$). In the morning, 45 µl of each sample was diluted into 1.5 ml of fresh M9 media and grown at 37 °C with shaking for another hour. 100 µl of each sample were then transferred into 6 wells of a 96-well plate (Greiner) at approximately 0.25 OD600. The plate was sealed with a Beath-Easy membrane (Merk), placed in an Infinite M Nano+ microplate reader (Tecan) and incubated at 37 °C with orbital shaking at 432 r.p.m. for five hours, with measurements of OD600 taken every 15 min. Every hour, the plate was taken out, the Breath-Easy membrane was removed and 10 µl of each sample was diluted into 1 ml of PBS for flow analysis. This was performed by using a MACS Quant flow cytometer, providing bacterial cell counts in parallel to OD600 measurements. Following sampling, the plate was placed back into the microplate reader and OD600 measurement resumed.

Growth rates, conversion factors and relation between ln(GI) and ln(C)

To infer the relation between GI and C, we analysed ln(GI) as a function of its correspondent ln(C) values. As discussed in Supplementary Note 1, the two variables scale linearly during the exponential phase of growth of the population of cells. Therefore, we applied the procedure briefly described here below and detailed in Supplementary Note 1 to quantify: i) the growth rates in the exponential phase, ii) CFs, and iii) the relation between ln(GI) and ln(C).

Briefly, the procedure for data analysis is based on the following points:

1. The C growth profiles, expressed as ln(C) vs time, are analysed and the region of fastest growth, i.e. the exponential phase of growth, is identified automatically (see Table I in Supplementary Note 1). The slope of the linear fit of the selected data is μ_c.
2. We selected the very same time-window in the corresponding growth profile ln(GI) vs time. The slope of this second fit is then μ_p (see Table II in Supplementary Note 1)
3. Finally, the data selected in previous steps 1) and 2) are fitted to obtain the relation between ln(GI) and ln(C) of the form $\ln(GI) = m*\ln(C) + q$, being m and q parameters of the linear fit (see Table III in Supplementary Note 1). From point 3. it follows that $GI = e^{(q)} * C^{(m)}$ and $C = (GI/\exp(q))^{(1/m)}$. All data were analysed through custom made scripts in *Wolfram Mathematica* (*version 13.1*). The code used for data analysis, description of it and source data file are available as Supplementary software file. See Supplementary Note 1 for further details.

Data exclusion
Outliers with GI < GI_0 or $C < C_O$, where C_O is the initial concentration of cells and GI_0 is GI normalised to zero at six hours were excluded. When cell count was performed in parallel to absorbance measurements, first GI measurements upon restarting the plate reader were discarded. GI growth curves with negative value for GI at six hours were excluded from the analysis.

Media acidification assay
RPMI and DMEM medium supplemented with 10% FBS were added to a 48-well plate. The following compounds doxo (1uM, Fisher Scientific), dox (2 ng/µl, Sigma), IPTG (1 mM, Sigma), Blast (0.5ug/ml, InvivoGen), Puro (1ug/ml, InvivoGen), HygB (50ug/ml, Sigma) and DMSO (0.1%, Invitrogen) were individually added to both media at T0 before running the plate reader assay for seven days.

Doxorubicin assay
HT1080 and K562 cells were plated into a 48-well plate at 10^5 cells/ml. The plate reader assay was started and let run for 24 hours. The plate was then removed from the microplate reader and 0 to 1 µM doxo (Fisher Scientific) was added to the plate. The plate was then placed back into the microplate reader and absorbance measures were performed for six more days. Cell count was performed in parallel every 24 hours.

Colchicine assay
Jurkat cells were plated into a 48-well plate according to the plate reader assay which was started for 24 hours. The plate was then removed from the microplate reader and cells were treated with 0 or 0.025ug/ml colchicine (Sigma). The plate reader assay was then resumed for six more days with parallel cell count was performed every 24 hours.

EBFP and mCherry expression assay
To assess for crosstalk between phenol red and fluorescence readings, HEK293TLP-EBFP and HEK293TLP-mCherry cells were plated in DMEM with and without induction (2 ng/µl dox, Sigma) in a 48-well plate grown first in the incubator. Two days post induction for HEK293TLP-mCherry cells or three days post induction for HEK293TLP-BFP cells, the plate was removed from the incubator, DMEM from half of the samples was gently removed and replaced with clear FluoroBrite DMEM (Gibco A1896701), and the plate was placed into the microplate reader to measure fluorescence levels [EBFP ($\lambda_{ex} = 381$, $\lambda_{em} = 445$) and mCherry ($\lambda_{ex} = 565$, $\lambda_{em} = 610$)]. The plate was then removed from the microplate reader and cells were counted using a Nucleocounter NC-250™ (Chemometec). To follow EBFP expression over time, HEK293TLP-EBFP cells were plated into a 48-well plate according to the plate reader assay and treated with 0 to 2 ng/µl dox (Sigma) to induce EBFP expression. The plate was then placed into the microplate reader and the assay started. Every six hour, following Abs_{430} and Abs_{560} measurements, EBFP fluorescence was also recorded for seven days.

Statistical analysis
A two-sided t-test was used to assess the statistical significance of *CF* resulting from different growing conditions, μ_{cp}, and fluorescent proteins expression levels.

Reporting summary
Further information on research design is available in the Nature Portfolio Reporting Summary linked to this article.

Data availability
All source data for the data sets and Fig.s presented in the manuscript are available in the source data file published alongside this manuscript. Constructs are available upon request to the corresponding authors. Plasmid maps of integrated constructs are available within the source data file. Source data are provided with this paper.

Code availability
The code used for data analysis is freely available as a Supplementary software file and data analysis is described in Supplementary Note 1.

References

1. James, J. S. et al. Automation and expansion of EMMA assembly for fast-tracking mammalian system engineering. *Acs Synth. Biol.* **11**, 587–595 (2022).
2. Kramme, C. et al. An integrated pipeline for mammalian genetic screening. *Cell Rep. Methods* **1**, 100082 (2021).
3. Di Blasi, R., Zouein, A., Ellis, T. & Ceroni, F. Genetic toolkits to design and build mammalian synthetic systems. *Trends Biotechnol*, https://doi.org/10.1016/j.tibtech.2020.12.007 (2021).
4. Chao, R., Mishra, S., Si, T. & Zhao, H. Engineering biological systems using automated biofoundries. *Metab. Eng.* **42**, 98–108 (2017).
5. Hillson, N. et al. Building a global alliance of biofoundries. *Nat. Commun.* **10**, 2040 (2019).
6. Kurokawa, M. & Ying, B. W. Precise, High-throughput Analysis of Bacterial Growth. *J. Vis. Exp.* https://doi.org/10.3791/56197 (2017).
7. Hall, B. G., Acar, H., Nandipati, A. & Barlow, M. Growth rates made easy. *Mol. Biol. Evol.* **31**, 232–238 (2014).
8. Stevenson, K., McVey, A. F., Clark, I. B. N., Swain, P. S. & Pilizota, T. General calibration of microbial growth in microplate readers. *Sci. Rep.* **6**, 38828 (2016).
9. Kumar, N. & Borth, N. Flow-cytometry and cell sorting: an efficient approach to investigate productivity and cell physiology in mammalian cell factories. *Methods* **56**, 366–374 (2012).
10. Dittami, G. M., Sethi, M., Rabbitt, R. D. & Ayliffe, H. E. Determination of mammalian cell counts, cell size and cell health using the Moxi Z mini automated cell counter. *J. Vis. Exp.* https://doi.org/10.3791/3842 (2012).
11. Carvell, J. P., Thomson, K. M. A new automated cell counter for mammalian cell culture assessment. *BMC Proc.* **9**, https://doi.org/10.1186/1753-6561-9-S9-P51 (2015).
12. Vega-Avila, E. & Pugsley, M. K. An overview of colorimetric assay methods used to assess survival or proliferation of mammalian cells. *Proc. West Pharm. Soc.* **54**, 10–14 (2011).
13. Molder, A. et al. Non-invasive, label-free cell counting and quantitative analysis of adherent cells using digital holography. *J. Microsc* **232**, 240–247 (2008).
14. Fracassi, C., Postiglione, L., Fiore, G. & di Bernardo, D. Automatic control of gene expression in mammalian cells. *Acs Synth. Biol.* **5**, 296–302 (2016).
15. Busschots, S., O'Toole, S., O'Leary, J. J. & Stordal, B. Non-invasive and non-destructive measurements of confluence in cultured adherent cell lines. *MethodsX* **2**, 8–13 (2015).
16. Odeleye, A. O. O., Castillo-Avila, S., Boon, M., Martin, H. & Coopman, K. Development of an optical system for the non-invasive tracking of stem cell growth on microcarriers. *Biotechnol. Bioeng.* **114**, 2032–2042 (2017).
17. Lanigan, T. M. et al. Real time visualization of cancer cell death, survival and proliferation using fluorochrome-transfected cells in an IncuCyte((R)) imaging system. *J. Biol. Methods* **7**, e133 (2020).
18. Shekhar, S., Karipott, S. S., Guldberg, R. E. & Ong, K. G. Magnetoelastic sensors for real-time tracking of cell growth. *Biotechnol. Bioeng.* **118**, 2380–2385 (2021).
19. Aijaz, A., Trawinski, D., McKirgan, S. & Parekkadan, B. Non-invasive cell counting of adherent, suspended and encapsulated mammalian cells using optical density. *Biotechniques* **68**, 35–40 (2020).

20. Seita, A., Nakaoka, H., Okura, R. & Wakamoto, Y. Intrinsic growth heterogeneity of mouse leukemia cells underlies differential susceptibility to a growth-inhibiting anticancer drug. *Plos One* **16**, e0236534 (2021).
21. Michl, J., Park, K. C. & Swietach, P. Evidence-based guidelines for controlling pH in mammalian live-cell culture systems. *Commun. Biol.* **2**, 144 (2019).
22. Rovati, L., Fabbri, P., Ferrari, L. & Pilati, F. Construction and evaluation of a disposable pH sensor based on a large core plastic optical fiber. *Rev. Sci. Instrum.* **82**, 023106 (2011).
23. Magnusson, E. B., Halldorsson, S., Fleming, R. M. & Leosson, K. Real-time optical pH measurement in a standard microfluidic cell culture system. *Biomed. Opt. Express* **4**, 1749–1758 (2013).
24. Yus, E. et al. Impact of genome reduction on bacterial metabolism and its regulation. *Science* **326**, 1263–1268 (2009).
25. Broto, A., Gaspari, E., Miravet-Verde, S., Dos Santos, V. & Isalan, M. A genetic toolkit and gene switches to limit Mycoplasma growth for biosafety applications. *Nat. Commun.* **13**, 1910 (2022).
26. Andersson, L. C., Nilsson, K. & Gahmberg, C. G. K562-a human erythroleukemic cell line. *Int J. Cancer* **23**, 143–147 (1979).
27. Schneider, U., Schwenk, H. U. & Bornkamm, G. Characterization of EBV-genome negative "null" and "T" cell lines derived from children with acute lymphoblastic leukemia and leukemic transformed non-Hodgkin lymphoma. *Int J. Cancer* **19**, 621–626 (1977).
28. Rasheed, S., Nelson-Rees, W. A., Toth, E. M., Arnstein, P. & Gardner, M. B. Characterization of a newly derived human sarcoma cell line (HT-1080). *Cancer* **33**, 1027–1033 (1974).
29. Graham, F. L., Smiley, J., Russell, W. C. & Nairn, R. Characteristics of a human cell line transformed by DNA from human adenovirus type 5. *J. Gen. Virol.* **36**, 59–74 (1977).
30. P., B. P. a. H. Using Phenol Red to Assess pH in Long-Term Proliferation Assays. *BioTek Instruments, Inc.*, https://www.biotek.com/assets/tech_resources/SLAS%202018%20Phenol%20red-LR.pdf (2018).
31. Zhang, L. et al. Control of IgG glycosylation in CHO cell perfusion cultures by GReBA mathematical model supported by a novel targeted feed, TAFE. *Metab. Eng.* **65**, 135–145 (2021).
32. Alton, G. et al. Direct utilization of mannose for mammalian glycoprotein biosynthesis. *Glycobiology* **8**, 285–295 (1998).
33. Vergara, M. et al. Differential effect of culture temperature and specific growth rate on CHO cell behavior in chemostat culture. *Plos One* **9**, e93865 (2014).
34. Howard, G. R., Jost, T. A., Yankeelov, T. E. & Brock, A. Quantification of long-term doxorubicin response dynamics in breast cancer cell lines to direct treatment schedules. *PLoS Comput Biol.* **18**, e1009104 (2022).
35. Tacar, O., Sriamornsak, P. & Dass, C. R. Doxorubicin: an update on anticancer molecular action, toxicity and novel drug delivery systems. *J. Pharm. Pharm.* **65**, 157–170 (2013).
36. Zwelling, L. A. et al. HT1080/DR4: a P-glycoprotein-negative human fibrosarcoma cell line exhibiting resistance to topoisomerase II-reactive drugs despite the presence of a drug-sensitive topoisomerase II. *J. Natl Cancer Inst.* **82**, 1553–1561 (1990).
37. Albright, C. F. et al. Matrix metalloproteinase-activated doxorubicin prodrugs inhibit HT1080 xenograft growth better than doxorubicin with less toxicity. *Mol. Cancer Ther.* **4**, 751–760 (2005).
38. Mukhtar, E., Adhami, V. M. & Mukhtar, H. Targeting microtubules by natural agents for cancer therapy. *Mol. Cancer Ther.* **13**, 275–284 (2014).
39. Matreyek, K. A., Stephany, J. J. & Fowler, D. M. A platform for functional assessment of large variant libraries in mammalian cells. *Nucleic Acids Res* **45**, e102 (2017).
40. Beal, J. et al. Robust estimation of bacterial cell count from optical density. *Commun. Biol.* **3**, 512 (2020).
41. Moffat, A. D., Elliston, A., Patron, N. J., Truman, A. W. & Carrasco Lopez, J. A. A biofoundry workflow for the identification of genetic determinants of microbial growth inhibition. *Synth. Biol. (Oxf.)* **6**, ysab004 (2021).
42. Dudley, Q. M. et al. Biofoundry-assisted expression and characterization of plant proteins. *Synth. Biol. (Oxf.)* **6**, ysab029 (2021).
43. Wong, B. G., Mancuso, C. P., Kiriakov, S., Bashor, C. J. & Khalil, A. S. Precise, automated control of conditions for high-throughput growth of yeast and bacteria with eVOLVER. *Nat. Biotechnol.* **36**, 614–623 (2018).
44. Fonseca, J. P. et al. A toolkit for rapid modular construction of biological circuits in mammalian cells. *Acs Synth. Biol.* **8**, 2593–2606 (2019).
45. Martella, A., Matjusaitis, M., Auxillos, J., Pollard, S. M. & Cai, Y. EMMA: an extensible mammalian modular assembly toolkit for the rapid design and production of diverse expression vectors. *Acs Synth. Biol.* **6**, 1380–1392 (2017).
46. Holowko, M. B., Frow, E. K., Reid, J. C., Rourke, M. & Vickers, C. E. Building a biofoundry. *Synth. Biol. (Oxf.)* **6**, ysaa026 (2021).
47. Le, K. et al. Assuring clonality on the beacon digital cell line development platform. *Biotechnol. J.* **15**, e1900247 (2020).
48. Le, K. et al. A novel mammalian cell line development platform utilizing nanofluidics and optoelectro positioning technology. *Biotechnol. Prog.* **34**, 1438–1446 (2018).

Acknowledgements

This work was supported by the New Investigator Award no. WT102944 from the Wellcome Trust U.K. (WT102944 to A.G. and M.I.) and the Biotechnology and Biological Sciences Research Council (grant BB/V00882X/1 to A.G and F.C.). F.C., C.E.B. and C.B. acknowledge the support of the Royal Society International Exchanges 2018 Round 1 grant IES \R1\180027. The authors would like to thank *Matreyek* et al. for providing the HEK293T-LP cell line adopted in this work, Paul Freemont and Jose Jimenez for feedback on the manuscript.

Author contributions

A.G., M.I. and F.C. conceptualised the research. A.G., R.D.B., D.P., M.S. and Z.Y. performed the measurements. C.E.B. and C.B. performed modelling and mathematical analysis. A.G. and C.E.B. analysed the data. F.C., M.I. and C.B. contributed funding. A.G., C.E.B., C.B., M.I. and F.C. wrote the manuscript. All authors read and edited the manuscript.

Competing interests

The authors declare no competing interests.

Additional information

Supplementary information The online version contains supplementary material available at https://doi.org/10.1038/s41467-023-44396-4.

Correspondence and requests for materials should be addressed to Carla Bosia, Mark Isalan or Francesca Ceroni.

Peer review information *Nature Communications* thanks Sofija Semeniuk, and the other, anonymous, reviewer(s) for their contribution to the peer review of this work. A peer review file is available.

Supplementary Information

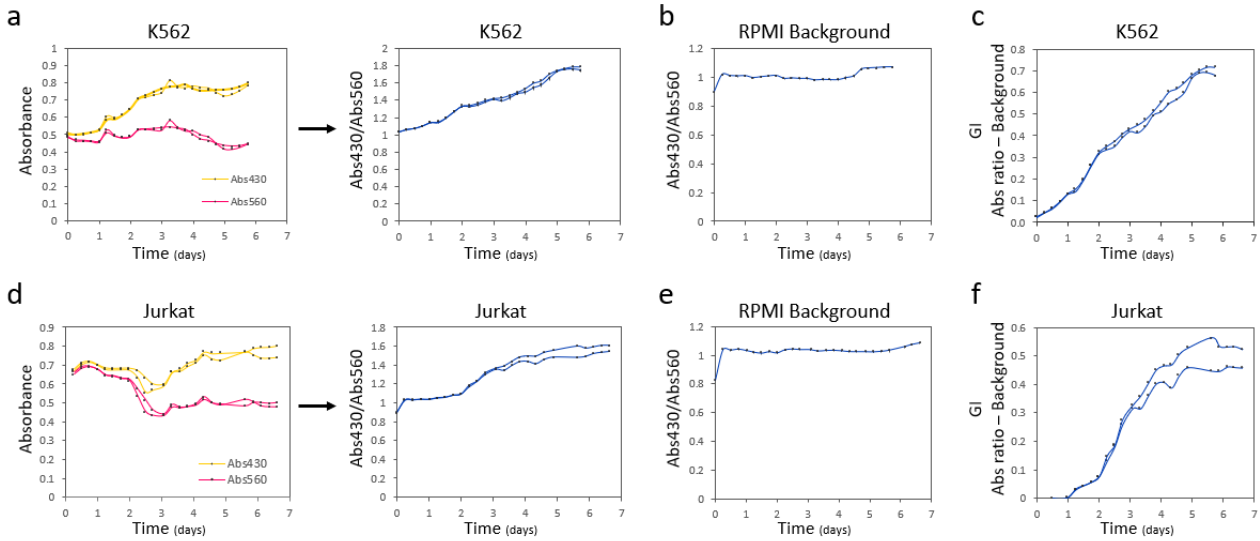

Figure S1. GI calculation for suspension cells from phenol red individual plate reader absorbance values. a) Representative duplicate variations of Abs_{430} (yellow) and Abs_{560} (pink) over time (left) for RPMI medium when K562 cells are cultured. Resulting Abs_{430} over Abs_{560} ratios (right, blue) over time. **b)** Average background and error of the mean for Abs_{430}/Abs_{560} ratio of RPMI over time (n=8) in control wells containing no cells. **c)** Representative duplicate GI profiles over time for K562 cells, resulting from Abs_{430}/Abs_{560} ratio normalised to RPMI background. **d)** Representative duplicates of Abs_{430} (yellow) and Abs_{560} (pink) over time (left) for RPMI medium over cultured Jurkat cells. Resulting Abs_{430} over Abs_{560} ratios (right, blue) over time. **e)** Background and error of the mean for Abs_{430}/Abs_{560} ratio of RPMI over time (n=8) in wells containing no cells. **f)** Representative duplicate GI profiles over time for Jurkat cells, resulting from Abs_{430}/Abs_{560} ratio normalised to RPMI background. Source data are provided as a Source Data file.

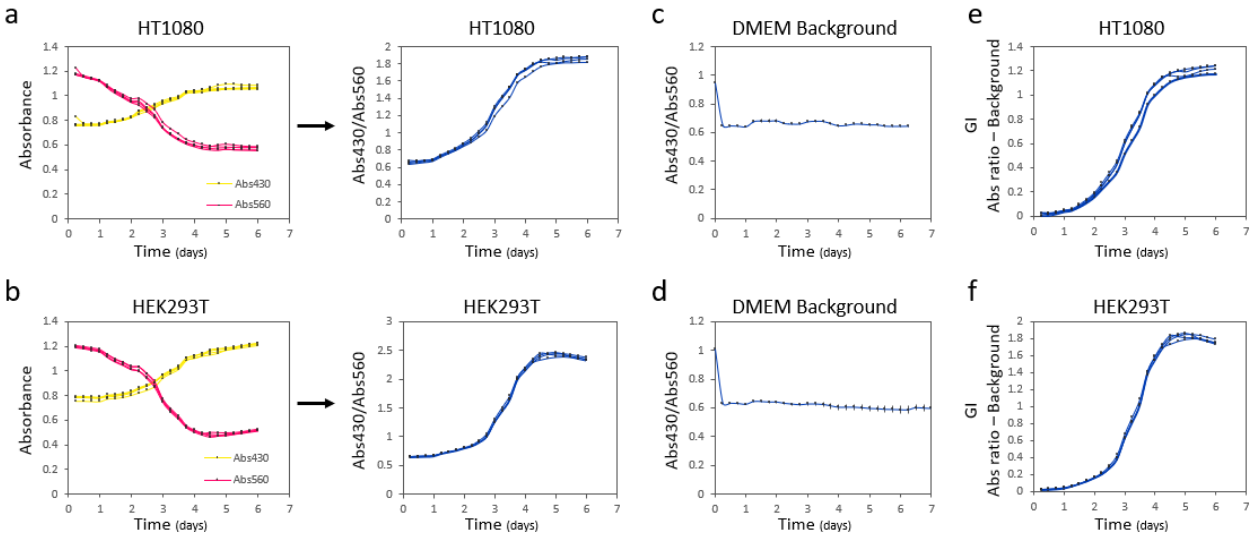

Figure S2. GI calculation for adhesion cells from phenol red individual plate reader absorbance values. Abs_{430} (yellow) and Abs_{560} (pink) over time (left) for DMEM medium when HT1080 **(a)** and HEK293T **(b)** cells are cultured. Resulting Abs_{430} over Abs_{560} ratio (right, blue) over time (n=4). Average background and error of the mean for Abs_{430}/Abs_{560} ratio of DMEM over time (n=3) in control wells containing no cells **(c**, **d)** GI profiles over time for HT1080 **(e)** and HEK293T **(f)** cells, resulting from Abs_{430}/Abs_{560} ratio normalised to DMEM background (n=4). Source data are provided as a Source Data file.

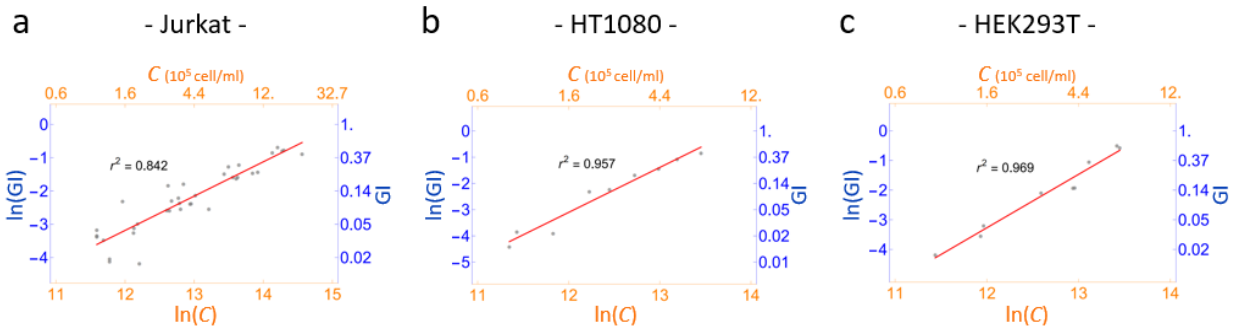

Figure S3. Linear relation of ln(GI) and ln(*C*) for Jurkat, HT1080 and HEK293T cells grown at 37°C with Glu. Graphs representing the relation between GI and *C* for **a)** Jurkat, **b)** HT1080 and **c)** HEK293T cells in logarithmic scale. The red solid line is the best fit of the data in linear region for which r^2 values are indicated. Linear fit equations are reported in Table S2. Numbers of biological repeats for each sample are reported in Table S3. Data analysis is described in the Methods section and in Supplementary Note 1. Source data are provided as a Source Data file.

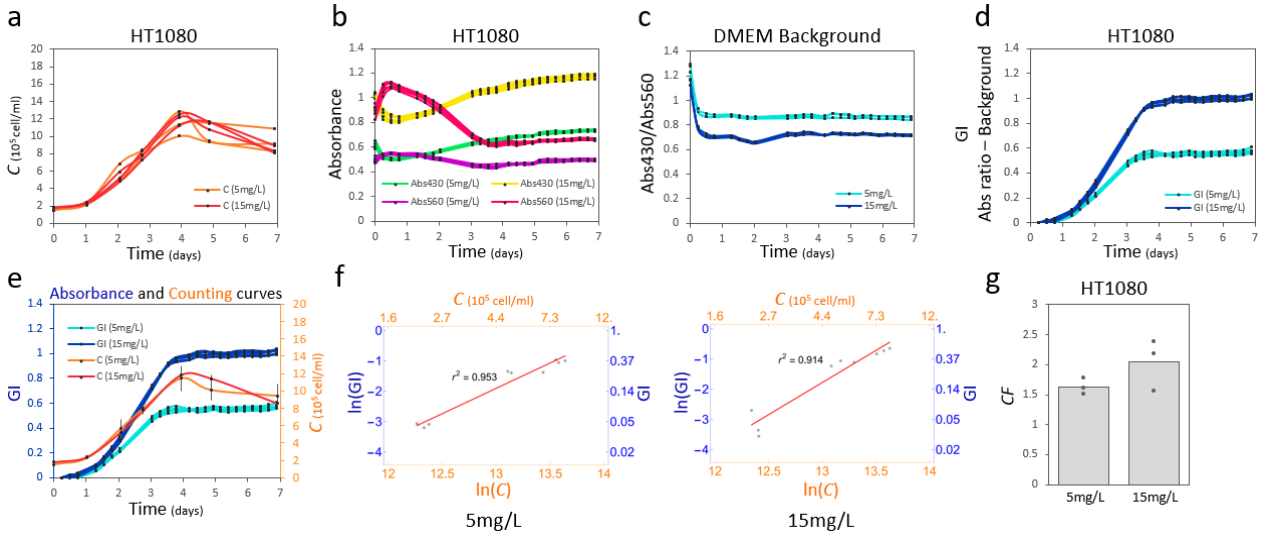

Figure S4. Effect of phenol red concentration on GI curves for HT1080 cells. a) Individual growth curves resulting from counting HT1080 cells cultured with 5mg/L (light orange) or 15mg/L (dark orange) phenol red (n=3). **b)** Overtime measure of Abs_{430} (green and yellow lines) and Abs_{560} (purple and pink lines) for HT1080 cells cultured in DMEM containing 5mg/L or 15mg/L phenol red (n=5). **c)** Overtime Abs_{430}/Abs_{560} ratio for DMEM background in control wells containing no cells in the presence of 5mg/L (light blue) or 15mg/L (dark blue) phenol red (n=3). **d)** GI profiles over time for HT1080 cells cultured in DMEM containing 5mg/L (light blue) or 15mg/L (dark blue) of phenol red (n=5). **e)** Representative growth curves resulting from phenol red acidification (GI, blue, left vertical axis) and averaged cell counts (*C*, orange, right vertical axis) of HT1080 cells cultured with 5mg/L (light blue and light orange) or 15mg/L (dark blue and dark orange) of phenol red (n=3). Numbers of biological repeats for each sample are reported in Table S3. For cell counts, data are presented as mean values +/- SD. **f)** Linear relation between ln(GI) and ln(*C*) for HT1080 cells when cultured in DMEM containing 5mg/L (left) or 15mg/L (right). The red line is the best fit of data within the linear region. Coefficient of determinations are indicated (r^2=0.914 for 5mg/L and r^2=0.953 for 15mg/L). **e)** Bar plot of CF for HT1080 cells cultured in DMEM containing either 5mg/L or 15mg/L phenol red. The height of the bar represents the mean value of the single replicates shown as black dots. All replicates can be found in Supplementary data file 1 while growth rate and CF are reported in Supplementary data file 2. Source data are provided as a Source Data file.

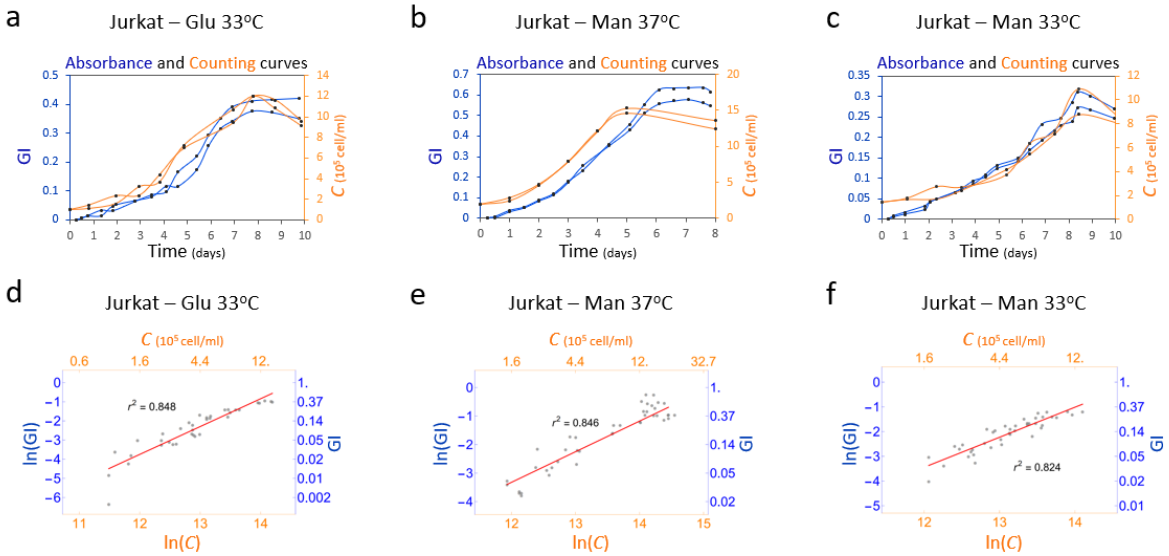

Figure S5. Growth of Jurkat suspension cells under different conditions can be characterised by a plate reader assay. Representative GI (blue, left vertical axis) and *C* (orange, right vertical axis) profiles over time for Jurkat cells grown with glucose (Glu) at 33ºC **(a)** or mannose (Man) at either 37ºC **(b)** or 33ºC **(c)**. All biological replicates can be found in Supplementary data file 1. Relation between GI and C for Jurkat cells grown in presence of Glu at 33ºC **(d)** or Man at either 37ºC **(e)** or 33ºC **(f)** in logarithmic scale. The red solid line is the linear fit of the data in the linear region for which r^2 values are indicated. Linear fit equations are reported in Table S2. Numbers of biological repeats for each sample are reported in Table S3. Data analysis is described in the Methods section and in Supplementary Note 1. Source data are provided as a Source Data file.

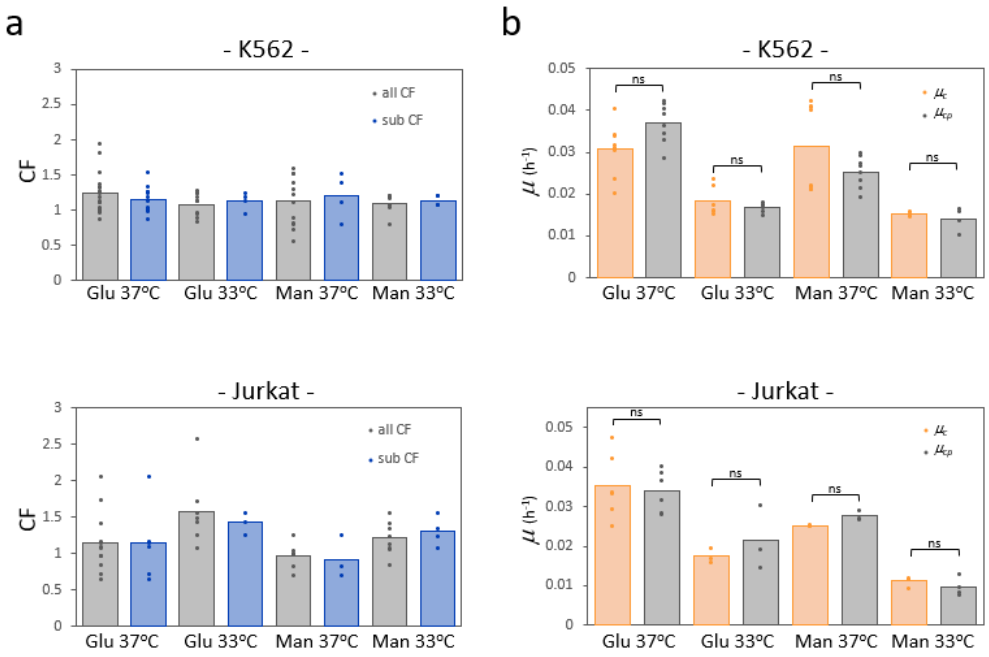

Figure S6. Reproducibility test of plate reader growth characterisation for K562 and Jurkat cells grown in different conditions. To test the automatable capability of our plate reader assay, the data set obtained for each growing condition was split. CF from one subset were averaged together (Table S5) to convert μ_p into μ_{cp} in the remaining data subset. **a)** Bar plots of all (grey) or a subset (sub, blue) of CF for K562 (top) and Jurkat (bottom) cells grown in presence of either glucose (Glu) or mannose (Man) at 37°C or 33°C. **b)** Bar plots of μ_c (orange) and μ_{cp} (grey), calculated as μ_p x CF average, for K562 (top) and Jurkat (bottom) cells grown in presence of either Glu or Man at 37°C or 33°C are shown. A two-sided t-test indicated that average CF of all or one subset are compatible ($p>0.05$) and that μ_{cp} are compatible with actual μ_c (ns, non-significant: $p>0.05$). The height of the bars represents the average value of the single replicates shown as dots. Numbers of biological repeats for each sample are reported in Table S3. Data analysis is described in the methods section and in Supplementary Note 1. Exact p values and source data are provided as a Source Data file.

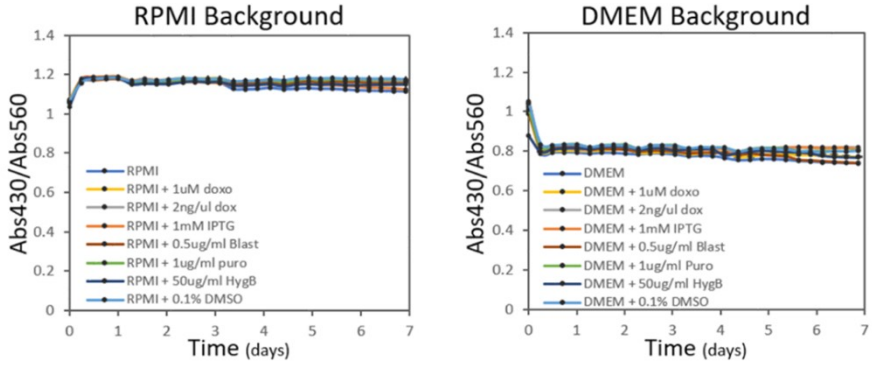

Figure S7. Compounds effect on media acidification. Average Abs_{430}/Abs_{560} ratios and +/- SEM over time of RPMI (left) and DMEM (right) medium supplemented with either 1uM doxorubicin (doxo), 2ng/µl doxycycline (dox), 1mM IPTG, 0.5ug/ml blasticidin (Blast), 1ug/ml puromycin (Puro), 50ug/ml hygromycin B (HygB) or 0.1% DMSO at T0 (n=4). Source data are provided as a Source Data file.

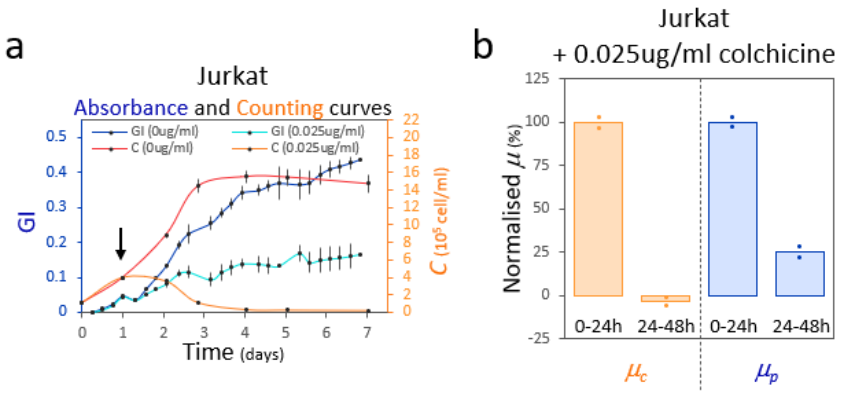

Figure S8. Jurkat cells treated with colchicine. Analysis of growth rate changes in Jurkat cells untreated (0ug/ml) or treated (0.025ug/ml) with colchicine added at 24h after the start of the assay (black arrow). **a)** Growth curves resulting from phenol red acidification (GI, blue, left vertical axis) and cell counts (*C*, orange, right vertical axis) of Jurkat cells cultured with colchicine 0ug/ml (dark blue and dark orange) or 0.025ug/ml (light blue and light orange) (n=4). Data are presented as mean values +/- SEM. **b)** Histograms of relative μ_c (orange, left) and μ_p (blue, right) values of Jurkat treated cells. Data show μ_c and μ_p for the 0-24 hours time window (preceding colchicine addition and for the 24-48 hours time window (after colchicine addition). Data were normalised to 100% growth rate in the 0-24 hours window. The height of the bar represents the mean value of the single replicates shown as dots. After colchicine addition, μ_c is decreased by ~100%, and μ_p is decreased by ~75%. -Growth rates are reported in Supplementary data file 2 while all replicates can be found in Supplementary data file 1. Source data are provided as a Source Data file.

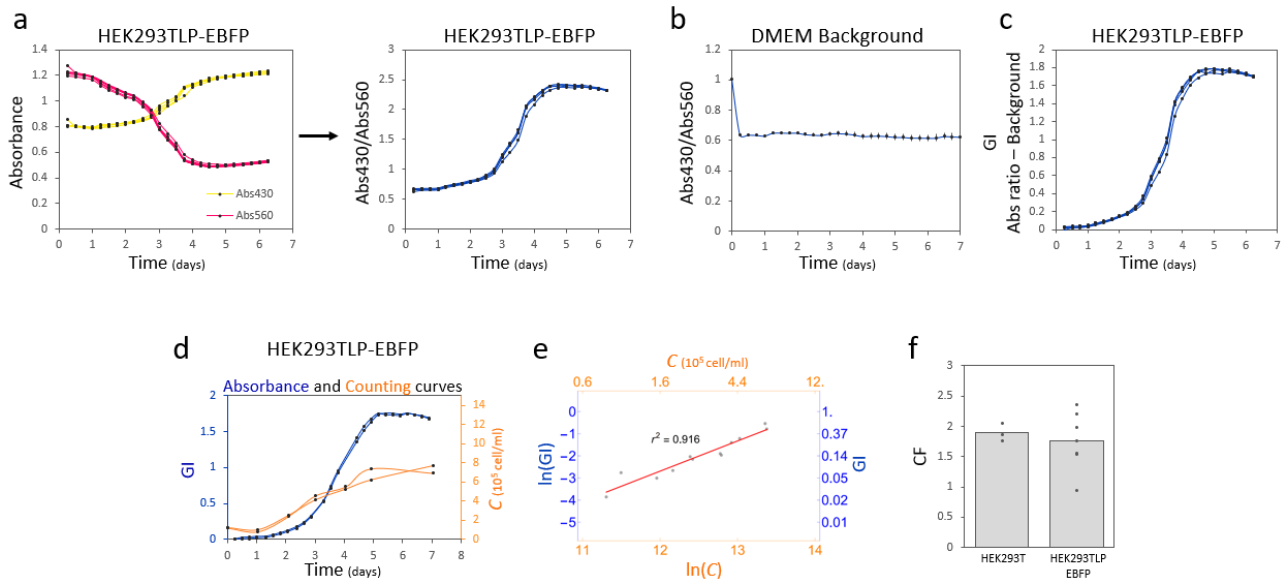

Figure S9. Growth of HEK293TLP-EBFP cells can be characterised with the plate reader-based assay. a) Abs_{430} (yellow) and Abs_{560} (pink) over time (left) for DMEM medium when HEK293TLP-EBFP cells are cultured. Resulting Abs_{430} over Abs_{560} ratio (right, blue) over time (n=4). **b)** Average background and error of the mean for Abs_{430}/Abs_{560} ratio of DMEM over time (n=3) in control wells containing no cells. **c)** GI profiles over time for HEK293TLP-EBFP cells, resulting from Abs_{430}/Abs_{560} ratio normalised to DMEM background (n=4). **d)** Representative growth curves resulting from phenol red acidification (GI, blue) and cell counts (*C*, orange). All biological replicates can be found in Supplementary data file 1. **e)** Relation between GI and *C* in logarithmic scale. Red solid line is the linear fit of the data in linear region for which r^2=0.916. The linear fit equations are reported in Table S2. **f)** Bar plot of CF for HEK293TLP-EBFP cells compared to their HEK293T parental cell line. The height of the bar represents the average value of the single replicates shown as black dots. Numbers of biological repeats for each sample are reported in Table S3. Data analysis is described in the Methods section and in Supplementary Note 1. Source data are provided as a Source Data file.

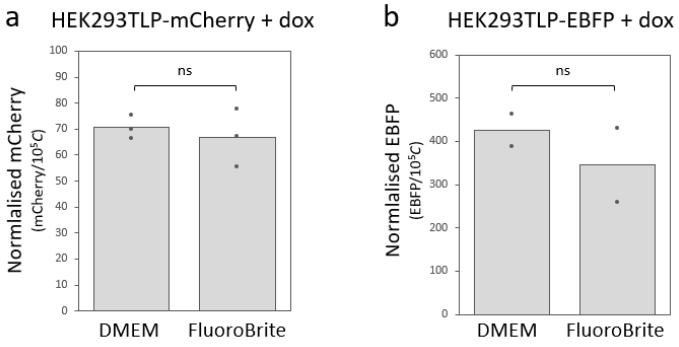

Figure S10. Fluorescence readout for mCherry and EBFP in presence and absence of phenol red in the medium. Cells were grown in the incubator with and without induction with 2ng/µl dox for 2 days **(a)** (mCherry, n=3) and 3 days **(b)** (EBFP, n=2). Cells were then resuspended in medium with (DMEM) and without (FluoroBrite) phenol red and fluorescence was measured at the plate reader. Cell counts were performed in parallel. A two-sided t-test indicated that average fluorescence level in DMEM and FluoroBrite are compatible (ns, non-significant: p>0.05). Data and statistical analysis are described in the Methods section. Raw values are reported in the source data file. Source data are provided as a Source Data file.

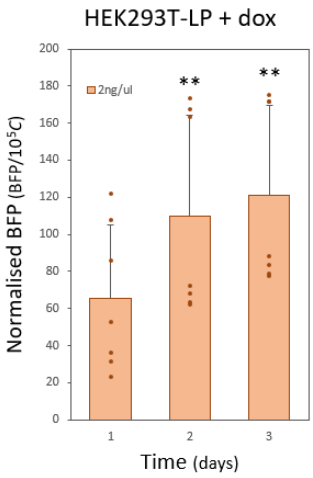

Figure S11. EBFP expression level in HEK293TLP-EBFP cells after dox induction. Bar plot of normalised fluorescence per cell (calculated as EBFP/10^5*C*) for HEK293TLP-EBFP cells induced with 2ng/µl dox over three days. Data are presented as mean values + SD with single replicates shown as dots. A two-sided t-test indicated that normalised EBFP levels increase significantly each day (**: $p<0.01$). Numbers of biological repeats for each sample are reported in Table S3. Data and statistical analysis are described in the Methods section. Exact p values and source data are provided as a Source Data file.

Supplementary tables

Cell line and growing condition	GI interval of linearity [GI_{min}; GI_{max}]	*C* interval of linearity [C_{min}; C_{max}] (10^5 cell/ml)
K562 Glu37°C	[0.034; 0.42]	[1.05; 10.9]
Jurkat Glu 37°C	[0.015; 0.51]	[1.08, 21.1]
HT1080 Glu 37°C	[0.012; 0.43]	[0.84; 6.95]
HEK293T Glu 37°C	[0.015; 0.61]	[0.93; 6.93]
HEK293TLP-EBFP Glu 37°C	[0.021; 0.59]	[0.81; 6.45]
K562 Glu 33°C	[0.022; 0.40]	[1.08; 10.3]
Jurkat Glu 33°C	[0.0018,0.39]	[0.975; 14.6]
K562 Man 37°C	[0.027; 0.24]	[0.92; 9.7]
Jurkat Man 37°C	[0.05; 0.43]	[2.38; 18.9]
K562 Man 33°C	[0.019; 0.24]	[1.08; 9.37]
Jurkat Man 33°C	[0.018; 0.305]	[1.73; 13.3]

TABLE S1. Intervals of linearity for each condition: region of fastest growth for *C* growth curves and corresponding values for GI growth curves.

Cell line and growing condition	Fit $\ln(GI) = m*\ln(C) + q$	r^2	Fit parameter ($q \pm err q$)	Fit parameter ($m \pm err m$)
K562 Glu 37°C	ln(GI) = 0.99*ln(C) - 14.6	0.893	(-14.6 ± 0.6)	(0.99 ± 0.04)
Jurkat Glu 37°C	ln(GI) = 1.03*ln(C) - 16	0.842	(-16 ± 1)	(1.03 ± 0.08)
HT1080 Glu 37°C	ln(GI) = 1.71*ln(C) - 23.6	0.957	(-23.6 ± 1.7)	(1.71 ± 0.14)
HEK293T Glu 37°C	ln(GI) = 1.80*ln(C) - 24.9	0.969	(-24.9 ± 1.5)	(1.80 ± 0.12)
HEK293TLP-EBFP Glu 37°C	ln(GI) = 1.36*ln(C) - 19.1	0.916	(-19.1 ± 1.6)	(1.36 ± 0.13)
K562 Glu 33°C	ln(GI) = 0.98*ln(C) - 14.7	0.752	(-14.7 ± 1.0)	(0.98 ± 0.08)
Jurkat Glu 33°C	ln(GI) = 1.45*ln(C) - 21.2	0.848	(-21.2 ± 1.4)	(1.45 ± 0.11)
K562 Man 37°C	ln(GI) = 0.87*ln(C) - 13.4	0.855	(-13.4 ± 0.8)	(0.87 ± 0.06)
Jurkat Man 37°C	ln(GI) = 1.07*ln(C) - 16.2	0.846	(-16.2 ± 1.3)	(1.07 ± 0.10)
K562 Man 33°C	ln(GI) = 1.01*ln(C) - 15.5	0.887	(-15.5 ± 0.7)	(1.01 ± 0.06)
Jurkat Man 33°C	ln(GI) = 1.21*ln(C) - 18.0	0.824	(-18.0 ± 1.2)	(1.21 ± 0.09)

TABLE S2. Results of the best fits for determining the relation between ln(GI) and ln(*C*) for all growing conditions with corresponding r^2 and mean parameter values +/- SEM.

	Number of biological repeats	
Cell line and growing condition	Plate reader	Cell counting
K562 Glu 37°C	20	20
Jurkat Glu 37°C	12	12
HT1080 Glu 37°C	3	3
HT1080 (15mg/L phenol red) Glu 37°C	3	3
HT1080 (5mg/L phenol red) Glu 37°C	3	3
HEK293T Glu 37°C	3	3
HEK293TLP-BFP Glu 37°C	7	7
K562 Glu 33°C	10	10
Jurkat Glu 33°C	7	7
K562 Man 37°C	12	12
Jurkat Man 37°C	6	6
K562 Man 33°C	8	8
Jurkat Man 33°C	8	8
HT1080 + doxo (0, 10, 25, 50, 75, 100, 500, 750 and 1000nM)	2-4 / [doxo]	2-4 / [doxo]
K562 + doxo (0, 10, 25, 50, 75, 100, 500, 750 and 1000nM)	4 / [doxo]	4 / [doxo]
HEK293T-LP + dox (0, 0.1, 0.25, 0.5, 1 and 2ng/µl)	7 / [dox]	-

Tables S3. Number of biological repeats per experiments with plate reader and cell counting protocol summary.

	Average ± err
K562 Glu 37°C	(1.24 ± 0.06)
Jurkat Glu 37°C	(1.15 ± 0.12)
HT1080 Glu 37°C	(1.76 ± 0.10)
HEK293T Glu 37°C	(1.89 ± 0.08)
HEK293T-LP Glu 37°C	(1.45 ± 0.18)

Tables S4. Average CF +/- SEM for cells grown at 37°C with Glu.

	Average of all CF	Average of CF subset
K562 Glu 37°C	(1.24 ± 0.06)	(1.16 ± 0.05)
K562 Glu 33°C	(1.09 ± 0.05)	(1.12 ± 0.06)
K562 Man 37°C	(1.13 ± 0.10)	(1.12 ± 0.16)
K562 Man 33°C	(1.10 ± 0.05)	(1.14 ± 0.04)
Jurkat Glu 37°C	(1.15 ± 0.12)	(1.14 ± 0.20)
Jurkat Glu 33°C	(1.58 ± 0.18)	(1.49 ± 0.06)
Jurkat Man 37°C	(0.96 ± 0.08)	(0.92 ± 0.17)
Jurkat Man 33°C	(1.21 ± 0.08)	(1.30 ± 0.10)

Tables S5. Average CF values +/- SEM across the different growing conditions of K562 and Jurkat cells.

Supplementary Note 1. Computational pipeline for automated data analysis

Content:

- **Computational pipeline for automated data analysis: Growth rates, conversion factors and relation between ln(GI) and ln(*C*).**
- **Pseudo-codes of algorithms developed for data analysis.**
- **On the relation between the linear fit of ln(GI) vs ln(*C*) and CF.**
- **Analysis of cells treated with doxo.**

Computational pipeline for automated data analysis: Growth rates, CF and relation between ln(GI) and ln(*C*).

The procedure that we adopted to obtain quantitative information relating plate reader and manual counts measurements of cell populations' growth originate from the following observation. Let's consider K562 growth curves measured both with manual counts (Fig. S12a) and the plate reader (Fig. S12b) expressed in logarithmic scale and binned every 50 hourslin (each colour of Fig. S12a-b represents a different temporal range). As time increases, first both ln(*C*) and ln(GI) increase their values covering almost all their range of variability in ~50 hours (this is the exponential phase of growth for both *C* and GI, red dots in Fig. S12a-c). Then, *C* saturates and decreases while GI only saturates (orange, green and blue dots). Therefore, as depicted in Fig. S12c, there is a temporal order in the way the data dispose in the plane ln(GI) vs ln(*C*): a first linear increase is then followed by a "simil-hysteresis" trend due to the different behaviour of the two quantities in the late growth phase. Based on this observation, we developed a method for quantifying i) the linear relation between ln(GI) and ln(*C*) that allows to convert measured GIs into cell concentrations, *C* and ii) the conversion factor (CF) that allows to convert growth rate measured in plate reader's growth curve (μ_p) into the growth rate obtained when cells are manually counted (μ_c).

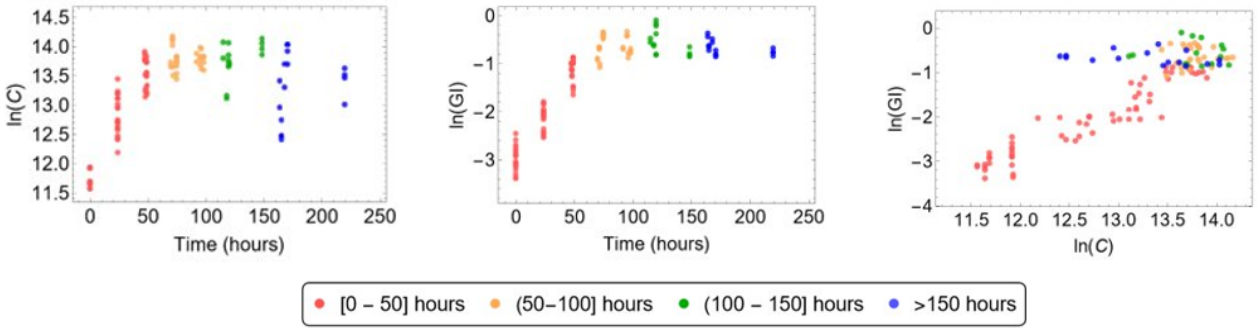

Figure S12. Measuring growth curves with manual counts and plate reader. Growth of K562 cells in Glucose at 37°C measured during time with **a)** manual counts and **b)** plate reader shown in logarithmic scale. Data are binned in time-windows of 50 hours, each colour represents one time-window. **c)** y-axis of panel b) (ln(GI)) as a function of the y-axis of panel a) (ln(*C*)). The data in the first 50 hours (in red) cover the region of fastest growth of curves in panel a) and correspond to the data shown in Figure 1d. Source data are provided as a Source Data file.

Our method is based on the three algorithms briefly described below (pseudo-codes in the following Tables I-III).

ALGORITHM 1 allows to select the time window corresponding to the fastest growth in manual counts growth curves and to compute the growth rate in such time-window. To do this, the algorithm: i) first performs linear fits of at least 3 consecutive points in sliding windows that start from time 0 and slide until the end of the growth curve (lines 1 – 10 in Table I). ii) Then, the algorithm selects the range of data points whose linear fit gives the maximum slope (line 12). In this way, the lower, the upper data limits, and the number of points to fit are optimized in the regression. The slope of the linear fit of these data points is the growth rate of the exponential phase (μ_c). This procedure is performed on curves obtained with manual counts and expressed in log scale, normalized to their initial value. The choice of having at least 3 data points has been based on the interest in estimating the average growth rate in the exponential phase and not the maximum growth rate. The latter, given the resolution of our manual counts, could be more easily biased by eventual experimental variability in cell counts. However, the supplied script for data analysis allows the user to choose the minimum number of data points on which to perform the fit.
In our analysis, such number (i.e., the parameter ***minNdata*** in Table I-III) has been set to 3 for all the growth conditions at 37°C, except for i) Jurkat Man 37°C where it was set to 4 and ii) Jurkat and K562 growing at 33°C where it was set to 5. The choice of the two values at points i) and ii) was driven by a longer duration of the exponential phase in the analysed conditions with respect to the other conditions.
Concerning data treated with doxo, the described procedure was applied to the data treated with all concentrations of doxo (by starting with at least 2, 3 or 4 data points, depending on the condition) except for HT1080 + doxo 1 μM. In this latter case, since the cells were almost not-growing, the automatic procedure was biased by fluctuations in cell counts. For this reason, we manually estimated the time window for calculating the growth rates as including the first 3 data points of each curve.
ALGORITHM 2 aims at computing the CF. For each growth curve measured with both *C* and GI, it relies on the outputs of *ALGORITHM 1* to i) first selecting the time points in GI growth curve that correspond to the fastest growth in *C* growth curve (lines 1,2 in Table II), then ii) it computes the growth rate in GI growth curve (μ_p) as the slope of the linear fit among such points (line 3), and finally iii) calculates the conversion factor CF = μ_p/μ_c (lines 4-5).

ALGORITHM 3 quantifies the linear relation between ln(GI) and ln(*C*) in their region of fastest growth. To do this, as *ALGORITHM 2* it i) first uses the output of *ALGORITHM 1* to identify the values of GI corresponding to the region of fastest growth in *C* growth curve (lines 1-6 in Table III) and then ii) computes the linear fit between ln(GI) and ln(*C*) (lines 7,8).

Pseudo-codes of algorithms developed for data analysis.

ALGORITHM 1. SELECTION OF GROWTH CURVE TIME POINTS CORRESPONDING TO THE FASTEST GROWTH

Inputs:
1. Normalized logarithmic growth curves C vs time, ***m*** time-points:
   dataC = (timeC, ln(C/C0))
2. ***minNdata*** = minimum number of data to fit.

Outputs:
1. ***idxμC*** = positions of time-points with the maximum slope
2. ***μC*** = value of the maximum slope
3. ***bestFit*** = best linear fit giving the maximum slope

Initialization of variables: assign 0 to variable ***i***

Initialization of matrices:

slopes = matrix of size (***ndata***) x (***ndata*** - ***ndataToadd***);

R2s = matrix of size (***ndata***) x (***ndata*** - ***ndataToadd***);

indexesfits = matrix of size (***ndata***) x (***ndata*** - ***ndataToadd***); # this will store the position of the first and the last data in the growth curve used for each fit.

```
ndataToadd = minNdata – 1;
while (i ≤ m) do
    for (j = ndataToadd to (m – i))
        indexesfits = (i, i + ndataToadd);
        select dataToFit = dataC at positions from i to (i + ndataToadd)
        linear fit of dataToFit;
        save the slope of the linear fit in the matrix slopes;
        save the R2 of the linear fit in the matrix R2s;
    end
end
μC = max(slopes);
IdxμC = find the indices in indexesfits corresponding to the fit with the maximum slope
return: IdxμC, μC
```

Table I: Pseudo-code for selecting the timepoints corresponding to the region of fastest growth in manual counts (*C*) growth curves and computing μ_c.

ALGORITHM 2. COMPUTE THE CONVERSION FACTOR

Inputs: ***1.*** First need to run ALGORITHM 1. ***Inputs for ALGORITHM 1:***

dataC = (timeC, ln(C/C0))

minNdata = minimum number of data to fit

2. ***dataInGI*** = (timeGI, ln(GI/GI0))

Note: For GI only time points corresponding to C must be considered.

Outputs: ***μC***, ***μP, CF***

1 Run ***ALGORITHM 1*** with ***dataC*** and ***minNdata*** as inputs.

2 Use the output ***IdxμC*** of ***ALGORITHM 1*** to select the time points of the growth curves GI corresponding to the maximum slope in C:
dataInGImaxSlope = dataInGI(***IdxμC***);

3 linearFit of ***dataInGImaxSlope***;

4 ***μP*** = slope of the linear fit;

5 ***CF*** = ***μP***/***μC***;

Table II: Steps for computing μ_p and the conversion factor (CF).

ALGORITHM 3. LINEAR RELATION BETWEEEN ln(GI) and ln(C)

Inputs: ***1.*** First need to run ***ALGORITHM 1***. ***Inputs for ALGORITHM 1:***

dataC = (timeC, ln(C/C0))

minNdata = minimum number of data to fit

2. ***dataC*** = (timeC, C)

3. ***dataGI*** = (timeGI, GI)

Note: For GI only time points corresponding to C must be considered.

Outputs: ***Linear fit ln(GI) vs ln(C), its r^2 and edges of the linear region (C_{min}, C_{max}, GI_{min}, GI_{max})***

1 Run ***ALGORITHM 1*** with ***dataC*** and ***minNdata*** as inputs.

2 Use the output ***IdxμC*** of ***ALGORITHM 1*** to select the C and GI values corresponding to the maximum slope in C:
CmaxSlope = dataC(***IdxμC***);
GImaxSlope = dataGI(***IdxμC***);

3 C_{min} = min(***CmaxSlope***); # lower bound for C in the region of linearity

4 C_{max} = max(***CmaxSlope***); # upper bound for C in the region of linearity

5 GI_{min} = min(***GImaxSlope***); # lower bound for GI in the region of linearity

6 GI_{max} = max(***GImaxSlope***); # upper bound for C in the region of linearity

7 LinearFit of ***dataInGIvsC*** = (ln(***CmaxSlope***), ln(***GImaxSlope***))

8 ***r^2*** = r^2 of the linear fit;

Table III: Steps for computing the linear relation between ln(GI) vs ln(*C*), its r^2, the boundaries of linearity.

On the relation between the linear fit of ln(GI) vs ln(*C*) and CF.

Since the linear relation between ln(GI) and ln(*C*) holds within the exponential phase, its slope can be directly related to CF. Indeed, according to our analysis, in the exponential phase of growth, the following expressions hold:

1. $\ln(C/C0) = a + \mu_C * t \rightarrow \ln(C) = a + \ln(C0) + \mu_C * t = a' + \mu_C * t$
2. $\ln(GI/GI0) = b + \mu_P * t \rightarrow \ln(GI) = b + \ln(GI0) + \mu_P * t = b' + \mu_P * t$
3. $\ln(GI) = m * \ln(C) + q$

From (1), $t = (\ln(C) - a')/\mu_C$ that substituted in (2) gives :

4. $\ln(GI) = (\mu_P/\mu_C)*\ln(C) + (b' - a' * \mu_P/\mu_C)$

From (3) and (4) it follows $m = \mu_P/\mu_C$ that corresponds to our definition of CF.
The compatibility between *m* and CF is shown in Figure S13a-c where, per each experiment discussed in Figure 1 and 2, points having as coordinates CF and *m* +/- its error obtained with the linear fit ln(GI) vs ln(*C*) lie on the bisector.

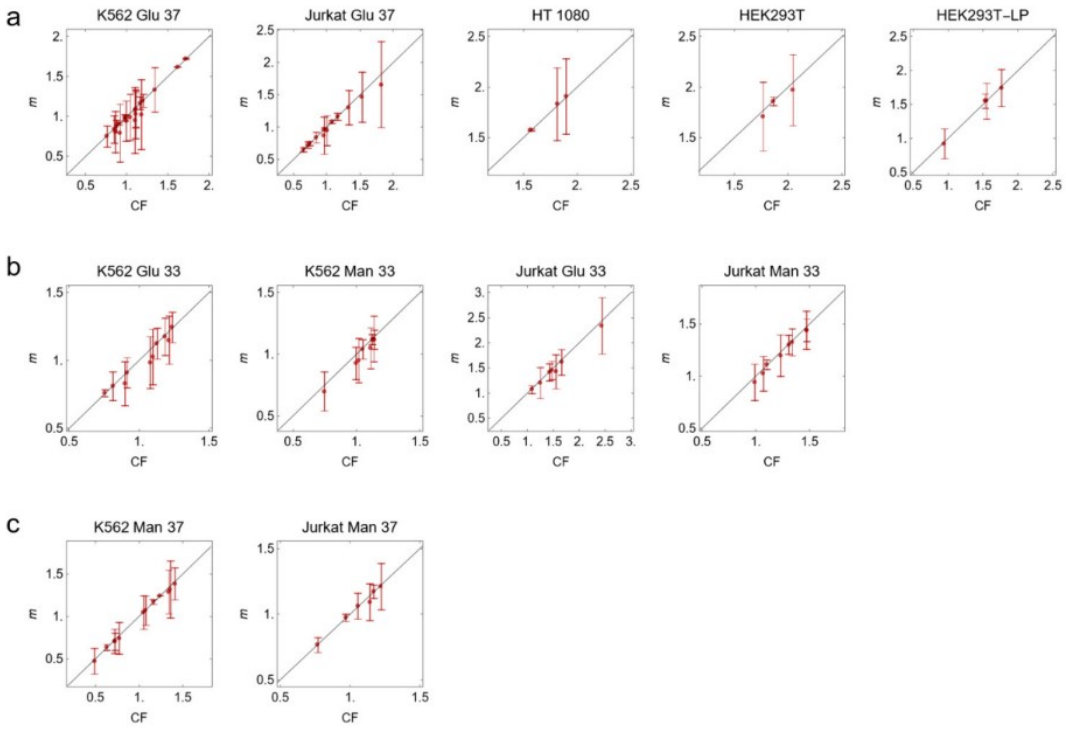

Figure S13. Relation between CF and *m* per each individual growth curve. The parameter *m* (+/- SEM) obtained from the linear fit of ln(GI) vs ln(*C*) and CF = μ_p/μ_c for each individual growth curve in red. In black is the bisector (i.e., *m* = CF). In all cases the bisector passes within the error bars. In **(a)** are the conditions analysed in Figure 1 of the main text together with HEK293T-LP; in **(b)** are the growth conditions at 33°C, in **(c)** K562 and Jurkat growing in Mannose (Man) at 37°C. Source data are provided as a Source Data file.

Thanks to this, CF found during the calibration of the studied cell line, can be used for calculating the growth rate within the exponential phase.

From (3) it follows that GI = exp(q)*C^m --> C = (GI/exp(q))^(1/m).

Analysis of cell lines treated with doxo.

To obtain the values shown in Figure 3c and 3d, we proceeded with the following three steps. First, we computed the growth rates in exponential phase with the analytic procedure we previously adopted in *Enrico Bena et al* [1]. Briefly, the growth curves measured with time resolution of 6 hours were fitted with a modified logistic function which parameters were the lag time, the exponential maximum growth rate and the level of saturation. Then, the edges of the exponential phase of growth were analytically determined as the intersection between the tangent to the fitted curve at the inflection point and the x-axis, as lower bound, and the horizontal line at the saturation level, as the upper bound. Then, the growth rate within the exponential phase was determined as the linear fit of the data within such phase.

Secondly, per each run, we computed the average growth rate of cells grown with 0 nM of doxo and thirdly, we normalized all the growth rates to the average value of the first run (Exp1) and expressed it in percentage.

Supplementary Note 2
Variability observed in CF and *m*

The calculated values of CF and *m* in the present work were characterised by some variability. To explain this, we would like to point the readers to our previously published work (*Enrico Bena et al. 2021*[1]), in particular Figure 3c where we considered the dependence of mammalian cells growth rate in exponential phase on the initial culture seeding concentration.
It was found that there exist a range of seedings, around to 10^5 cells/ml (which is exactly the recommended seeding for our cell lines and the one used for experiments presented in our manuscript), for which the variability in growth rates within the exponential phase (lambda_max) is maximum (in the figure each dot represents the maximum growth rate of a population of Jurkat cells and the same holds for K562 cells). This means that growth curves generated with that initial seeding will be highly variable in terms of maximal growth rate (much more than curves generated with lower seeding N_0, such as 10^3 cells/ml). If one used a few of these curves to generate the model and obtain CF, the variability in the growth rates will reflect on the amplitude of the error bar over the CF. Thus, experiments performed with initial seeding different by orders of magnitude must be considered as performed in different growth conditions, requiring initial characterisation as explained in the main manuscript.

From the above, we consider that for the seeding more widely adopted in lab-based experiments and advised by manufacturer`s instructions (~10^5 cells/ml) there exist an intrinsic variability. In our work we show how, besides this given intrinsic variability, we are able to measure CF, providing an easy and quick method for mammalian cell growth tracking that is less time consuming and provides higher throughput than traditional cell counting. The price to be paid is a confidence interval higher than that we would have in the case of lower seeding. On the contrary, for lower-seeding experiments, the price to be paid would be a much longer and variable lag time, leading to single growth experiments taking up to 20-30 days, as we previously showed. Please refer to Figure 2a in *Enrico Bena et al*[1] to see the plot displaying variability in the lag time, and thus in the overall experiment timeline, as a function of N_0.

Supplementary Note 3

Accuracy in converting GI into *C* compared to the accuracy in converting bacteria's OD into *C*.

To quantify the accuracy of our method in estimating cell concentration from absorbance measurements, we compared it to the accuracy in estimating bacteria concentration from OD_{600} measurements. In order to do so, we quantified the accuracy in cell concentration estimates as defined in *Beal et al*[2] and compared our results to those obtained there for bacteria. In *Beal et a*l, the authors defined the accuracy as the ratio between the estimated mean fluorescence per cell (fluorescence from *E. coli* normalised by calibrated OD measurements) and the mean fluorescence per cell measured by calibrated flow cytometry. We reasoned that, in our case, this would mean to compare the mean cell count predicted by our calibration method (C_p or $C_{predicted}$) to the mean cell count effectively measured (C or $C_{measured}$), which reduces to the ratio $A = C_{predicted}/C_{measured}$. The more A is close to 1, the better the method is in estimating cell counts. We thus built the linear model using a triplicate of growth curves for which we have both cell counts and absorbances, and then measured the accuracy as the mean A derived from all GI data within the exponential phase for three growth curves, different from those used to build the model. By repeating this procedure for 20 different combinations of growth curves, we found that on average A = (1.07 +/- 0.02) for K562 cells, in agreement with the accuracy of microsphere dilution method investigated for bacterial cells.

This result suggests that the accuracy of our method in estimating cell counts from absorbance measurements is equivalent to estimating cell counts from OD in bacteria culture.

To corroborate the robustness of our method, we tested the variability of A by changing the size of N, i.e., the number of curves used for constructing the calibration curve. Specifically, we repeated the above procedures by randomly choosing 2, 3, 5, 10 and 17 curves for the model and repeated the procedure 100 times per each condition. Figure S14 and Table S6 (below) show that increasing the number of curves used for the model helps in decreasing the dispersion of the accuracy values. However, when considering the coefficient of variation (CV) this is of the order of 0.1, varying from 0.13 (model with 2 curves) to 0.08 (model with 17 curves), suggesting that the large variability in CF and accuracy is intrinsic in the experimental working condition.

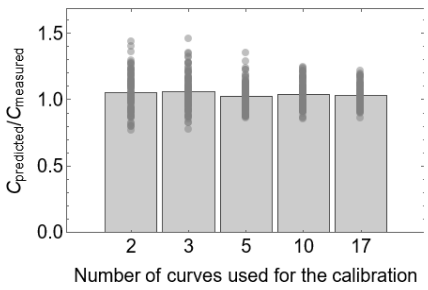

Figure S14. Comparison of the mean accuracies obtained by constructing the linear model with N = 2, 3, 5, 10, 17 curves. Dots are the average of $A = C$predicted/Cmeasured from 3 curves

randomly chosen from the pool of curves not used for the model. For each condition, 100 replicates have been run, each time with N + 3 curves randomly chosen from the entire pool of experiments. Bars are the average of the dots. Data are from K562 cells grown in Glu at 37°C.

N curves	A +/- err$A$	CV
2	1.052 +/- 0.014	0.13
3	1.059 +/- 0.013	0.12
5	1.026 +/- 0.010	0.097
10	1.040 +/- 0.010	0.093
17	1.030 +/- 0.008	0.079

Table S6. Mean A values, standard error of the mean (err$A$) and CV (i.e. the standard deviation of A over its mean) obtained by constructing the linear model with different number of curves.

Overall, these results show that our method is robust in predicting the concentration of cells within the exponential phase of growth of the population independently of the number of curves used to construct the calibration curve. Moreover, the accuracies in estimating the concentration of cells are similar to predicting bacteria counts from OD.

Additional manuscript supplementary data files

Supplementary data file 1. Plots of ln(GI) and ln(C) over time for all biological replicates.
Supplementary data file 2. Excel file of μ_p, μ_c and CF for all biological replicates.
Supplementary software file. *Wolfram Mathematica* code used for data analysis.
Instruction on how to use the code for data analysis.
Input data script for data analysis

Supplementary References

1 Enrico Bena, C. *et al.* Initial cell density encodes proliferative potential in cancer cell populations. *Sci Rep* **11**, 6101, doi:10.1038/s41598-021-85406-z (2021).

2 Beal, J. *et al.* Robust estimation of bacterial cell count from optical density. *Commun Biol* **3**, 512, doi:10.1038/s42003-020-01127-5 (2020).